NEURAL MANIFOLD REGULARIZATION: ALIGNING 2D LATENT DYNAMICS WITH STEREOTYPED, NATURAL, AND ATTEMPTED MOVEMENTS

Anonymous authors
Paper under double-blind review

ABSTRACT

Mapping neural activity to behavior is a fundamental goal in both neuroscience and brain-machine interfaces. Traditionally, at least three-dimensional (3D) latent dynamics have been required to represent two-dimensional (2D) movement trajectories. In this work, we introduce Neural Manifold Regularization (NMR), a method that embeds neural dynamics into a 2D latent space and regularizes the manifold based on the distances and densities of continuous movement labels. NMR pulls together positive pairs of neural embeddings (corresponding to closer labels) and pushes apart negative pairs (representing more distant labels). Additionally, NMR applies greater force to infrequent labels to prevent them from collapsing into dominant labels. We benchmarked NMR against other dimensionality reduction techniques using neural activity from four signal modalities: single units, multiunit threshold crossings, unsorted events, and local field potentials. These latent dynamics were mapped to three types of movements: stereotyped center-out reaching and natural random target reaching in monkeys, as well as attempted handwriting in a paralyzed patient. NMR consistently outperforms other methods by over 50% across four signal modalities and three movement types, evaluated over 68 sessions. Our code is uploaded.

1 INTRODUCTION

Ongoing breakthroughs in neural recording technologies have led to an exponential increase in the number of simultaneously recorded neurons. To interpret this high-dimensional neural data, manifold analysis has emerged as a promising population-level technique in both neuroscience (Cunningham & Yu, 2014; Jazayeri & Ostojic, 2021) and cognitive science (Beiran et al., 2023; Jurewicz et al., 2024). Analyzing neural manifolds helps to illuminate representations in both biological (Gardner et al., 2022; Hermansen et al., 2024) and artificial (Cohen et al., 2020; Chung & Abbott, 2021; Wang & Ponce, 2021; Dubreuil et al., 2022) neural networks. Because neural population dynamics are high-dimensional, dimensionality reduction methods are necessary to visualize low-dimensional latent dynamics. However, there is a trade-off between representation capacity and dimensionality.

Classical dimensionality reduction methods like principal components analysis (PCA) require eight to fifteen dimensions to represent a simple and stereotyped eight-direction center-out reaching task (Gallego et al., 2020; Gallego-Carracedo et al., 2022). Using the same dataset, state-of-the-art (SOTA) dimensionality reduction methods achieve even better performance using only four dimensions (Zhou & Wei, 2020; Schneider et al., 2023). However, since only 3D spaces are directly visible, these studies have to either display the four dimensions in two separate figures (Zhou & Wei, 2020) or manually remove one dimension (Schneider et al., 2023) to visualize the data. In both cases, further reducing the dimensionality of these low-dimensional latent dynamics is necessary. In a 3D latent space, eight groups of latent dynamics are clearly visible. Unfortunately, the reaching trajectories cannot be identified from the latent dynamics, even when the latent dynamics are trained to align with reaching trajectories (Schneider et al., 2023).

Many hand movement trajectories, such as center-out reaching, random target reaching (O'Doherty et al., 2017; Lawlor et al., 2018), and handwriting (Willett et al., 2021), occur within a 2D physical space. Arguably, the ultimate goal of dimensionality reduction methods is to reveal—either unsu-

pervised or supervised—2D latent dynamics that are well-aligned with, or even indistinguishable from, movement trajectories. However, a 2D latent space has significantly less representational capacity than a 3D latent space. For body movements within 2D physical spaces like open field arenas, W-shaped mazes, figure-8 mazes, or radial arm mazes, previous dimensionality reduction methods such as Uniform Manifold Approximation and Projection (UMAP) (McInnes et al., 2018) require a 3D latent space to avoid overlap in their latent dynamics (Gardner et al., 2022; Tang et al., 2023; Yang et al., 2024). To our knowledge, no studies have demonstrated the successful use of 2D latent dynamics to represent 2D movement trajectories.

Here, we focus on neural-behavioral analysis, particularly hand movements, which have been extensively studied. We chose hand movement tasks as a testbed for dimensionality reduction methods because: 1) multi-channel recordings provide the necessary high-dimensional data for dimensionality reduction, 2) the diversity of hand movement tasks enables testing different types of task labels, 3) long-term recordings across months and years allow for testing model consistency, 4) a variety of neurophysiological signal types are available, and 5) public open-source datasets enable benchmarking across models. We extended our method to body movement tasks to assess its generalizability.

2 Related work and our contributions

There are at least **five categories** of dimensionality reduction methods:

Linear methods: These include techniques like PCA, jPCA (Churchland et al., 2012), demixed PCA (dPCA) (Kobak et al., 2016), and preferential subspace identification (PSID) (Sani et al., 2021). PCA captures the majority of variance in the data, jPCA reveals rotational dynamics in monkey reaching, dPCA further isolates task-related components, and PSID can extract latent dynamics that predict motion during reach versus return epochs.

Nonlinear methods: Techniques such as UMAP and t-distributed stochastic neighbor embedding (t-SNE) (Van der Maaten & Hinton, 2008) are widely used in biological data, such as identifying different neuron cell types (Lee et al., 2021). While these methods can reveal distinct identities, they often collapse temporal dynamics that resemble neural activity. UMAP, when combined with labels, has been used for dimensionality reduction (Schneider et al., 2023; Zhou & Wei, 2020).

Generative methods using recurrent neural networks (RNNs): Models such as fLDS (Gao et al., 2016), latent factor analysis via dynamical systems (LFADS) (Pandarinath et al., 2018), AutoLFADS (Keshtkaran et al., 2022), and RADICaL (Zhu et al., 2022) have been shown to better model single-trial variability in neural spiking activity compared to PCA. However, these methods often rely on restrictive explicit assumptions about the underlying data statistics.

Label-guided generative methods using variational autoencoders (VAEs): Methods such as Poisson identifiable VAE (pi-VAE) (Zhou & Wei, 2020), SwapVAE (Liu et al., 2021), and targeted neural dynamical modeling (TNDM) (Hurwitz et al., 2021; Kudryashova et al., 2023) fall into this category. For instance, pi-VAE uses eight reaching directions as labels to structure the latent embeddings, resulting in eight well-separated latent dynamics in M1.

Contrastive learning methods: Recently, contrastive learning has been introduced for learning robust, generalizable representations of neural population dynamics. Examples include CEBRA (Schneider et al., 2023) and Mine Your Own vieW (MYOW) (Azabou et al., 2021). When trained with hand trajectories, CEBRA demonstrates the most disentangled latent dynamics compared to pi-VAE and AutoLFADS; however, these latent dynamics are not aligned with the actual hand trajectories.

Our specific contributions are as follows:

1. Introduction of NMR: A dimensionality reduction method that regularizes latent neural embeddings based on label distances and densities. NMR leverages the continuous nature of movement labels to extract disentangled neural manifolds and addresses label imbalance by applying a pushing force inversely related to the frequency of rare labels. NMR is the first to address imbalanced labels for time-series neural data, and also the first to do so without adding or removing any data samples.

2. Simplification of contrastive regularizer (ConR) loss: NMR replaces the NCE (noise-contrastive estimation) loss used in the CEBRA (Schneider et al., 2023) with a significantly simplified version of the ConR loss (Keramati et al., 2023). The original ConR loss involved six hyperparameters that

required fine-tuning for each session. Our modified ConR loss simplifies this by reducing it to a single temperature hyperparameter. While the original ConR loss showed marginal improvements of less than 5% over previous models, our modified version outperforms CEBRA by over 50%.

3. Evaluation across modalities and movements: We evaluate NMR against CEBRA and pi-VAE using four modalities of neural signals and three types of movements. No previous studies have evaluated dimensionality reduction techniques on LFP signals or attempted to visualize latent dynamics during attempted movements. NMR outperforms the other methods under all conditions.

4. Stability and generalizability across time and monkeys: We assess the stability of our models across months using the same training parameters, as well as their generalizability across monkeys. NMR demonstrates the highest stability over time and superior decoding performance across monkeys, even when using the same set of parameters.

3 MODEL

3.1 MOTIVATION: CONTINUOUS AND IMBALANCED LABELS IN CONTRASTIVE LEARNING

Contrastive learning involves three types of samples: an anchor (or reference sample), positive samples, and negative samples. Positive samples, also known as augmented samples, share the same label as the anchor but are generated by applying transformations to the anchor, such as rotation, flipping, cropping. For time-series data, such as neural dynamics, positive (or augmented) samples are often created by selecting time-offset samples from the anchor, preserving temporal relationships. The goal of contrastive learning is to train the model to bring positive samples closer to the anchor in the latent space while pushing negative samples farther away, effectively learning representations that capture meaningful similarities and distinctions.

The contrastive learning-based method CEBRA outperforms other dimensionality reduction techniques for neural-behavior data analysis. However, it has two key limitations when applied to continuous behavioral data, such as movements. First, CEBRA does not take advantage of the fact that movements are continuous; instead, it treats movement locations or velocities as discrete classes, similar to how images are handled (Fig 1b, left). Second, CEBRA fails to account for the highly imbalanced distribution of movement positions or velocities (Fig 1a-c). In each reach trial, velocities are near zero, and hand positions are close to the center (0, 0) at the start and end of movements, while large velocities or distant hand positions are rare. Such imbalanced distributions are common in real-world data (Yang et al., 2021) and differ significantly from manually curated and balanced datasets like ImageNet (Deng et al., 2009). In the neuroscience field, **previous studies have either neglected the issue of imbalanced labels or downsampled the frequent labels**(Appendix A.1).

3.2 MODIFIED AND SIMPLIFED LOSS FUNCTION FROM CONR

Our loss function was modified from the original ConR, which has six hyperparameters. First, there is the temperature τ for regularizing feature similarity, which we kept as the only hyperparameter in our studies. Second, the distance threshold ω determines whether paired samples are positive or negative; we replaced this with the median value of pairwise distances (Fig 1e). Third, the pushing power η, which should depend on the sample distribution, was manually assigned in their code for all datasets; we removed this parameter. Fourth, there was an additional temperature e used for regularizing label distance in their code, which was not mentioned in the paper. We unified this by using the same temperature τ mentioned earlier. Fifth and sixth were α and β, used for regularizing the regression and contrastive losses, respectively. Since we did not compute the regression loss, we removed these two hyperparameters as well. In summary, we only used the single hyperparameter τ, and our model performed well and robustly across the 68 sessions of data we evaluated.

Our NMR model utilizes the same feature encoder as CEBRA, ensuring that the extracted neural embeddings are identical in both models (Appendix A.2). To integrate the ConR loss into CEBRA, we also modified the data sampling strategy. In CEBRA, each training epoch consists of three batches of samples: anchor, positive, and negative. The positive batch is created with a fixed time offset (e.g., 1 or 10 ms) from the anchor, while the negative batch is uniformly sampled from the entire time series. To compute the ConR loss, we utilize the same anchor and positive batches extracted by CEBRA. **The samples in the positive batch will be classified as positive, negative,**

or discarded (Fig. 1d), depending on the difference between the ground truth and predicted labels, as well as the threshold for label distance (details provided in the next section). While CEBRA only requires continuous labels once to determine the indices of the positive batch, NMR retains the continuous labels and reuses them in the ConR loss. The negative batch is no longer needed. It is important to note that NMR does not alter the neural embeddings or labels, nor does the modified sampling strategy introduce any additional neural data or labels.

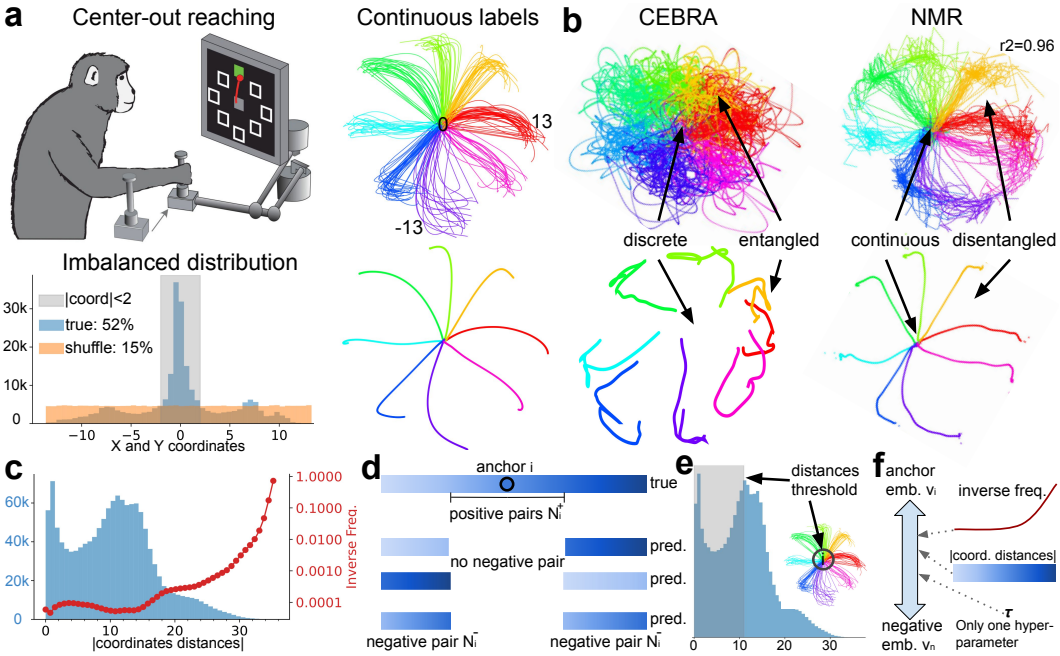

Figure 1: NMR introduces a novel loss function to map 2D latent dynamics with 2D stereotyped hand movements. **a** A monkey performs a center-out reaching task in eight equally spaced directions (modified from Perich et al. (2018)). All reaches start from the center, located at the (0, 0) X-Y coordinates. The slower speed at the beginning of the movement and the central starting point contribute to a highly imbalanced distribution of coordinates around (0, 0). The shuffled data histogram shows the same number and range of values as the true coordinates but follows a uniform distribution. **b** CEBRA extracts latent dynamics that are misaligned with movements (original figures from CEBRA paper). In contrast, NMR extracts latent dynamics that are closely aligned with movement trajectories, making them nearly indistinguishable.. **c** The count (Y-axis, left) and inverse frequency (Y-axis, right) of pairwise distances between X and Y coordinates. Only 10 percent of the coordinates from the figure above are shown. **d** Smooth gradients of blue represent continuous labels. **e** The distance threshold is set to the median of all absolute coordinate distances in each batch. Since half the data have distances less than 2, potential negative samples will exist outside the gray circle. **f** The pushing force between anchor embeddings and negative embeddings in the feature space is determined by the inverse frequency of label distances, the label distances, and the sole hyperparameter in our model: temperature. Fig 10 demonstrates the stability of latent dynamics, the latent dynamics extracted by PCA, and the latent dynamics of ablation studies.

3.3 New Loss function for CEBRA

Although NMR does not alter the neural embeddings in the anchor and positive batches or introduce new labels, it predicts labels using linear regression based on the anchor batch and its labels. Fig. 1d illustrates how positive and negative pairs are selected based on true labels (1st row), predicted labels (2nd to 4th rows), and the distance threshold (horizontal line below the 1st row) (Appendix A.3). Samples with distances to an anchor below a specified threshold (1st row, colorbar within the horizontal line) are classified as positive pairs, regardless of their predicted labels. Samples far from the anchor (2nd to 4th rows, six colorbars outside the horizontal line) are either discarded (2nd and 3rd rows) or classified as negative pairs (4th row), depending on their predicted labels.

Samples in the 2nd and 3rd rows are discarded because their predicted labels (represented by very dim or dark blue colors) are far from the anchor, irrespective of whether the prediction is correct (2nd row) or incorrect (3rd row). In contrast, samples in the 4th row are considered negative pairs because their predicted labels (medium blue) are closer to the anchor than the threshold, i.e., distant samples have been mispredicted as nearby samples. Similar to the original ConR loss, the label distance is calculated using the $L1$ distance, which is the sum of the absolute differences between the X-coordinates, Y-coordinates, and hand reach angles of any paired labels. **Although our initial sampling approach mirrors that of CEBRA, during the computation of the ConR loss we improve negative sampling by selecting samples supervised by labels, and we improve positive sampling by filtering out unintended negative samples** (Fig 8, Appendix A.4).

Let $d(\cdot,\cdot)$ represent the distance measure between two labels. The ground truth sample label is y and predicted sample label is $\hat{y}$. For each anchor sample i, the positive samples are those that satisfy $d(y_i, y_p) < \hat{d}$, the negative samples are those that satisfy $d(y_i, y_n) > \hat{d}$ and $d(\hat{y_i}, \hat{y_n}) < \hat{d}$, where $\hat{d}$ is the median of all pairwise distance shown in Fig 1e.

Let's denote v_i, v_p, and v_n as the neural embeddings of corresponding true labels of y_i, y_p, and y_n. N_i^+ is the number of positive samples, N_i^- is the number of negative samples. $K_i^+ = \{v_p\}_p^{N_i^+}$ is the set of embeddings from positive samples, $K_i^- = \{v_n\}_n^{N_i^-}$ is the set of embeddings from negative samples. $sim(\cdot,\cdot)$ is the similarity measure between two feature embeddings (e.g. negative L_2 norm). For each anchor i whose neural embedding is v_i, true label is y_i, and loss is:

$$\mathcal{L} = \frac{1}{N_i^+} \sum_{v_j \in K_i^+} -\log \frac{\exp(sim(v_i, v_j)/\tau)}{\sum_{v_p \in K_i^+} \exp(sim(v_i, v_p)/\tau) + \sum_{v_n \in K_i^-} S_{i,n} \exp(sim(v_i, v_n)/\tau)} \quad (1)$$

where τ is a temperature hyperparameter and $S_{i,n}$ is a pushing weight for each negative pair shown in Fig 1f:

$$S_{i,n} = \frac{1}{p_{d(y_i,y_n)}} exp(d(y_i, y_n)\tau) \quad (2)$$

where $\frac{1}{p_{d(y_i,y_n)}}$ is the inverse frequency of labels distances distribution shown in Fig 1c. The final loss is the summed and averaged loss $\mathcal{L}$ over all anchors i in a batch. Mathematical details of NMR and CEBRA models are presented in the Appendix A.7.

The performance gain of NMR over CEBRA (Figure 1b) can be attributed to two factors. First, NMR uses multiple positive pairs (K_i^+), whereas CEBRA uses only a single positive pair. Second, the pushing weight $S_{i,n}$ for the negative pairs, as mentioned earlier. We conducted ablation studies (Figure 10d, e) and found that using multiple versus one positive pair has negligible improvement on the alignment of latent dynamics and decoding performance (explained variance of movements, 0.95 vs. 0.96). In contrast, when the pushing weight for negative pairs is set to one, the latent dynamics are squeezed—that is, large but infrequent values are collapsed into small but frequent values (0.42 vs. 0.96). This is precisely what NMR aims to resolve. Therefore, it is the pushing weight $S_{i,n}$ applied to the negative pairs that contributes to the improved performance.

4 EXPERIMENTS

Two common ways to evaluate dimensionality reduction methods are: (1) the qualitative direct visualization of the revealed latent dynamics, and (2) the quantitative decoding performance of task variables using a decoder. The decoding performance is measured by the explained variance (r^2) between the ground truth and the decoded movement trajectories. Although better decoding performance can be achieved with complex decoders, we choose to enforce a linear mapping across the three methods to prevent excessively complex decoders from compensating for poor latent dynamics estimation (Pei et al., 2021). **Decoding performance is a metric but not the ultimate goal!** Therefore, our dimensionality reduction method combined with a linear regression decoder should not be directly compared with other decoders. Furthermore, movement decoding from raw neural signals without dimensionality reduction that preserves all the information in the neural data, when paired with a linear regression decoder, actually has worse performance (0.73 vs. 0.96). When PCA is combined with a linear regression decoder, the performance is significantly worse (Fig 10a-c, 0.34).

We evaluated NMR against the self-supervised learning-based models CEBRA and pi-VAE. These models were chosen because they (1) represent two categories—contrastive and generative—of dimensionality reduction methods that have achieved SOTA performance; (2) have released their code and use publicly available datasets; and (3) benchmark against previous models such as PCA, UMAP, fLDS, LFADS, AutoLFADS, and others. **We evaluated all three models using the same neural data and movement labels** (see Appendix A.5 and Table 1 for training parameters). To eliminate bias from using data from a single session in a single brain area—where pi-VAE and CEBRA were previously tested—we conducted experiments across a total of 68 sessions (Appendix A.6). These experiments involved neural signals from four modalities: M1, PMd, and S1 in monkeys, and the precentral gyrus in humans. Importantly, we included three different movement tasks. While our primary focus is on hand movements, we also evaluated body movements using neural data from the rat hippocampus. The results demonstrated a 37% improvement of NMR over CEBRA (Fig. 9).

4.1 NMR Explains the Largest and Most Consistent Variance of Stereotyped Movements Using Single Neuron Data

Our initial focus was on classical stereotyped center-out reaching tasks, similar to the task in Fig 1, but with neural data from the motor cortex (M1) and premotor cortex (PMd) instead of the somatosensory cortex (S1). We found that NMR significantly outperformed hyperparameter-optimized CEBRA and pi-VAE models by a large margin (M1: 0.88 vs 0.48 vs 0.43; PMd: 0.9 vs 0.53 vs 0.37, median values, Fig 2). The performance difference between NMR and CEBRA was statistically significant (M1, t = 14.9, p = 6.3e-10; PMd, t = 16.8, p = 1e-8; paired t-test with multiple comparisons correction), as was the difference between NMR and pi-VAE (M1, t = 9.7, p = 2.4e-7; PMd, t = 9.8, p = 2.8e-6). Importantly, NMR exhibited less variability across sessions (M1, 0.03; PMd, 0.02, standard deviation) compared to both CEBRA (M1, 0.1; PMd, 0.06) and pi-VAE (M1, 0.18; PMd, 0.18). Multiple runs with different parameters within the same session showed that CEBRA is more

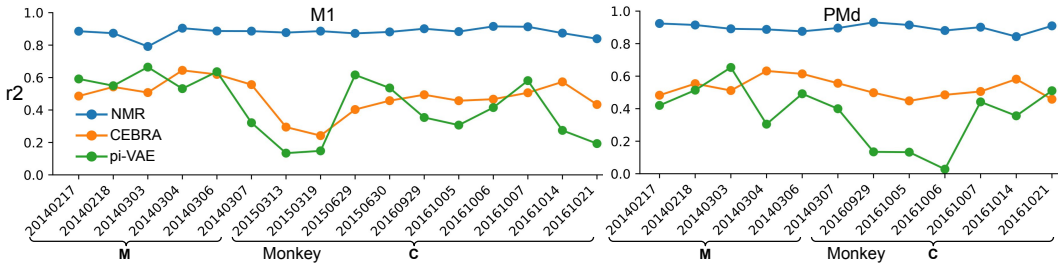

Figure 2: NMR consistently outperforms CEBRA and pi-VAE across different brain areas, monkeys, and hemispheres. The Y-axis displays the explained variance, while the X-axis shows the session dates (formatted as YYYYMMDD) for 16 sessions in M1 and 10 sessions in PMd. Data from six sessions in 2014 (M1 or PMd) are from Monkey M, four sessions in 2015 (M1) are from the right hemisphere of Monkey C, and six sessions in 2016 (M1 or PMd) are from the left hemisphere of Monkey C. Task labels represent hand velocity. The best hyperparameters were chosen when evaluating the CEBRA and pi-VAE models. Model parameters were kept fixed across all 28 sessions. Figs 1112 illustrate the hyperparameter search and stability of the CEBRA and pi-VAE models, respectively, while Fig 13 shows the results using 3D CEBRA and pi-VAE models.

robust than pi-VAE (Figs 1112), consistent with previous findings from the CEBRA paper. Since CEBRA and pi-VAE typically perform better at higher dimensionality, we also compared 2D NMR with 3D CEBRA/pi-VAE (i.e., without further dimensionality reduction using PCA on the original 3D output). The results remained similar (Fig 13). In summary, NMR explained the largest variance of hand movements and demonstrated the most consistent performance across sessions.

4.2 NMR Achieves Superior Decoding Performance Within and Across Sessions, Subjects, and Years

Since NMR explains the largest movement variance (r^2) across all sessions in both M1 and PMd, we further investigated whether the latent dynamics aligned with movements in one session could be utilized to decode movements in other sessions or even across different subjects (Appendix A.8).

Fig 3 shows the within-session decoding performance (values on the diagonal) and cross-session decoding performance (values off the diagonal) for the three models. Consistent with the explained variance results, NMR significantly outperformed CEBRA (t = 11.5, p = 2.4e-8, paired t-test with multiple comparisons correction) and pi-VAE (t = 6.2, p = 5e-5) in decoded variance within sessions. The performance gap was even more pronounced for cross-session decoding, with NMR performing nearly twice as well as CEBRA (t = 18.5, p = 1.5e-47) and six times better than pi-VAE (t = 21, p = 1.4e-55). Additionally, CEBRA almost tripled the performance of pi-VAE (t = 9.6, p = 3.6e-18). These results are consistent with the smaller cross-session standard deviation observed in the Fig 2.

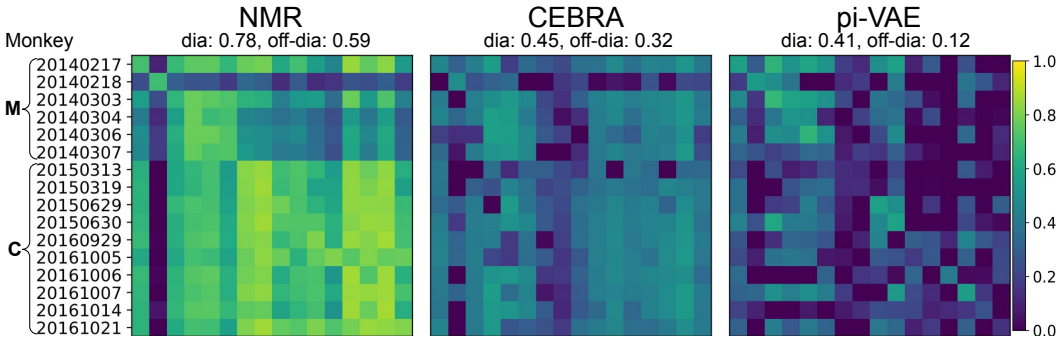

Figure 3: Within- and across-session movements decoding performance (r^2) in M1 for Monkey M and C. Fig 14 shows the decoding results in PMd. Appendix A.8 shows the technical details.

Interestingly, we did not find a causal relationship between the variability of decoding performance and the number of neurons or trials in each session (Table 2). The variability is unlikely due to neural signals, as the within-session decoding performance of Monkey M on 20140218 is similar to that of five other sessions. The variability is highly likely due to movement changes, as Monkey M on 20140218 had the worst cross-session decoding performance in both M1 and PMd (Fig 14), despite having more neurons than on 20140307 (M1: 38 vs. 26; PMd: 121 vs. 66). In summary, the low-dimensional, high-performance, and stable movement-aligned latent dynamics revealed by NMR enable effective neural decoding across sessions and even across different subjects.

4.3 Dimensionality Reduction Using Bands of Local Field Potential Signals

Dimensionality reduction methods have predominantly been evaluated on single-neuron data, either through neurophysiological recordings or calcium imaging. However, numerous studies have demonstrated that local field potential (LFP) signals contain movement-related information and can achieve comparable decoding performance to single-neuron data. To explore this further, we tested three models using the LFP signals that accompanied the previous single-neuron recordings.

We first examined whether different bands of LFP signals were modulated by movement (Fig 4a). As expected, movement onset, occurring approximately 300 ms after the go cue, evoked amplitude changes in several LFP bands. Notably, LFP bands across different channels showed distinct modulations, a prerequisite for population decoding and for revealing latent dynamics from high-dimensional neural data. The local motor potential (LMP), which consists of unfiltered and smoothed LFP signals, exhibited the most diverse movement modulation across all channels. We then evaluated the explained variance (Fig 4b) and decoding performance (Fig 16) of NMR and CEBRA across 28 sessions in three representative LFP bands. The results showed that performance was LFP band-dependent: the LMP and high-frequency band (200-400 Hz) significantly outperformed the middle-frequency band (12-25 Hz). Furthermore, NMR outperformed CEBRA across all three bands—LMP (0.79 vs 0.46), Gamma (0.74 vs 0.44), and Beta (0.36 vs 0.22)—with statistically significant differences (t = 6.8, 7.8, and 3.1; p = 1.8e-5, 3.8e-6, and 0.002, paired t-test with multiple comparisons correction) in both M1 and PMd. However, we observed some variability. NMR's performance dropped below CEBRA in certain bands and sessions (e.g., LMP in Monkey C, 20161006, M1). In contrast to the results with single-neuron data, NMR showed greater variability across sessions (0.15 vs 0.11, 0.2 vs 0.09, 0.23 vs 0.17). Despite this, the overall performance of LFP signals

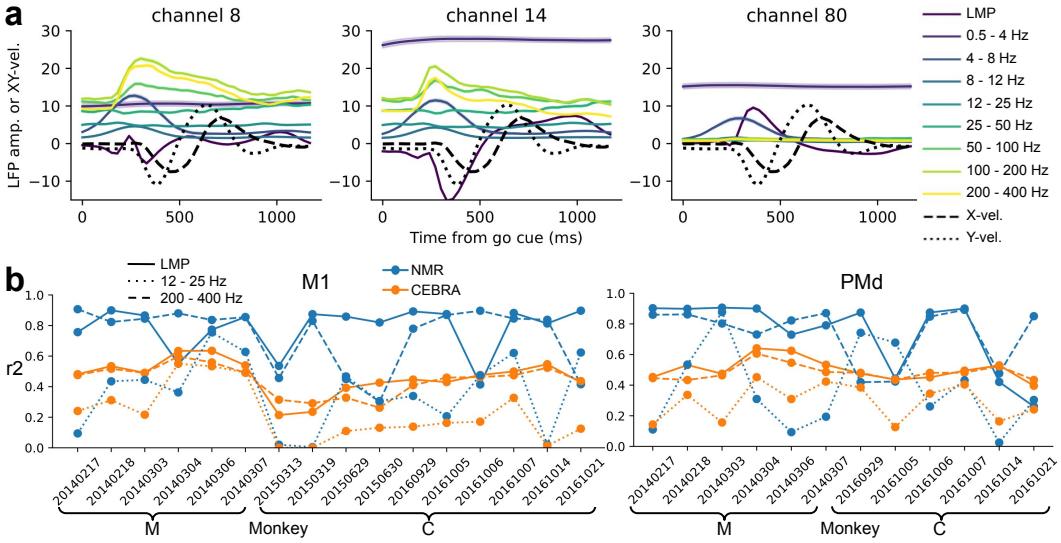

Figure 4: Dimensionality reduction on LFPs. **a** Seven LFP bands along with X- and Y-velocity in three example channels. Error bars represent the standard error of the mean across all trials in this session (Monkey C, 20161014, M1). **b** The explained variance (r^2) of the model is shown across all sessions in M1 (left) and PMd (right) for three LFP bands: LMP, 12-25 Hz Beta band, and 200-400 Hz Gamma band. Figs 15 and 16 show the hyperparameter tuning of the two models and the decoding performance on test trials, respectively.

was only slightly lower than that of single-neuron data. In summary, NMR outperforms CEBRA even when using LFP signals, though it exhibits more variability across sessions.

4.4 NMR Outperforms Other Models on Natural Movements Using Both Single-Neuron and Unsorted Events Data

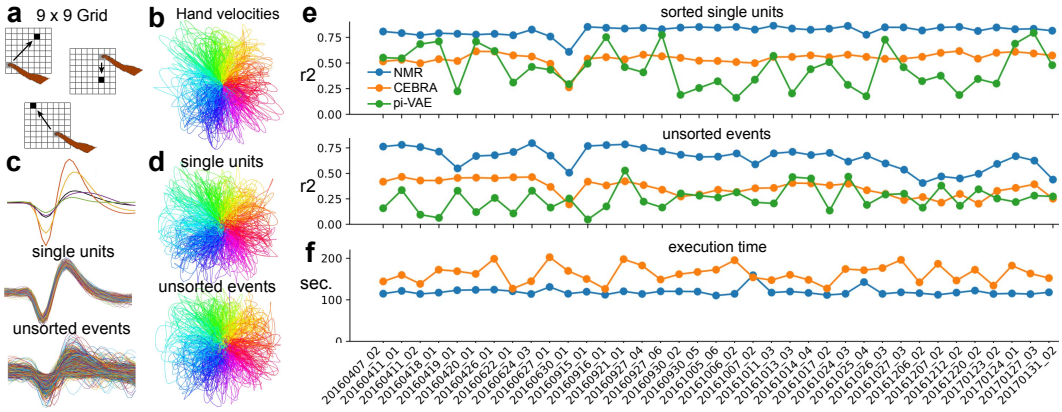

Figure 5: Dimensionality reduction on natural movements using data from single units and unsorted events. **a** Three example movement trials in a 9 x 9 grid on a computer screen (modified from Keshtkaran et al. (2022)). **b** Hand velocities for all reaching movements, with different colors representing different angles. Data are from session indy 20170124 01. **c** Four sorted single units and the remaining unsorted events from one channel. **d** 2D latent dynamics revealed by NMR using both sorted and unsorted data modalities. **e** Explained variance for three models across 37 sessions using sorted single units (top) and unsorted events (bottom). **f** Execution time for NMR and CEBRA, with pi-VAE excluded for comparison since it runs on the CPU instead of the GPU. Figs 171819 show findings with different hyperparameters, decoding performance for test trials with 3D models, and execution time under varying conditions, respectively.

Our previous evaluation, while exhaustive, focused primarily on stereotyped movements. It is important to assess how NMR performs in natural movements without predefined target locations. To address this, we benchmarked three models in a task involving restricted natural movements, where target locations appeared randomly on a 9 x 9 grid on the screen (Fig 5a). In this task, there is no delay period, and trials have variable lengths with almost no overlap in movement trajectories (Fig 5b). Each recording channel contained one or more sorted single units as well as unsorted remaining events (Fig 5c). Surprisingly, both sorted single units and unsorted events were able to uncover movement (velocity)-aligned 2D latent dynamics (Fig 5d).

We benchmarked the three models across 37 sessions over a span of 10 months in one monkey. Consistent with the results from 28 sessions in the center-out reaching task, NMR outperformed CEBRA and pi-VAE by a large margin in all sessions for both sorted single units (0.82, 0.55, and 0.45) and unsorted events (0.65, 0.36, and 0.25) (Fig 5e). Hyperparameter tuning across all 37 sessions for all three models further supported these conclusions (Fig 17). We observed consistent results on the test trials and when using 3D versions of CEBRA and pi-VAE models (Fig 18). Since CEBRA computes the distance between an anchor and all samples in the batch, while NMR does not compute distances for predicted labels that deviate from the true labels, we hypothesized that NMR would have more efficient computing than CEBRA. Supporting this hypothesis, we found that execution time across sessions was significantly shorter for NMR compared to CEBRA, both for single units (119 vs 163 seconds, t = 12, p = 3e-14) (Fig 5f) and for unsorted events (149 vs 166 seconds, t = 3.5, p = 0.001) (Fig 19a). This result held true under different hyperparameters for both models (Fig 19b, c). In summary, NMR demonstrates superior performance for natural movements using data from both single units and unsorted events.

In the previous task, natural movements on a 9 x 9 grid involved unpredictable yet predefined target locations. However, in more realistic scenarios, a target can appear anywhere. To simulate this, we further evaluated the three models on a free natural movements task, where the target could appear at any location on the screen (Fig 6a). NMR revealed 2D latent dynamics that were better aligned with both hand velocity and direction compared to CEBRA (0.88 vs 0.79, Fig 6b). We ran 20 evaluations to compare the performance and stability of the models. Consistent with previous findings, NMR achieved the highest performance (0.79, 0.58, and 0.56) in explaining hand velocities and exhibited the smallest variability across runs (0.002, 0.004, and 0.117) (Fig 6c). Similar trends were observed in the test trials, where NMR showed higher performance (0.77, 0.65, and 0.53) and lower variability (0.005, 0.006, and 0.109) (Fig 20). Additionally, NMR had a shorter execution time compared to CEBRA (146 vs 165 seconds, t = 3.5, p = 0.0025, Fig 20).

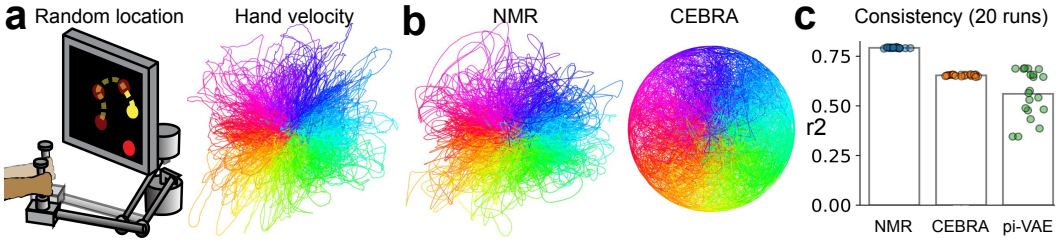

Figure 6: Dimensionality reduction on natural movements with random target locations. **a** A monkey was trained to perform sequences of four reaches to randomly placed target locations (modified from Safaie et al. (2023)). The colors of each reaching trial indicate the angles. **b** 2D latent dynamics revealed by NMR and CEBRA. **c** Explained variance of hand velocities by three models across 20 runs. Fig 20 provides additional details on decoding performance and execution time.

4.5 NMR Maps Latent Dynamics to Attempted Center-Out Handwriting

The datasets evaluated so far come from 67 sessions across three different hand-reaching tasks in four macaque monkeys. However, two key questions remain: Can NMR work for attempted or imagined reaching instead of physical hand movements? And how does it perform outside of monkeys? To address these questions, we focused on a dataset involving attempted center-out handwriting in 16 directions by a paralyzed patient. One significant challenge in this task is the absence of measurable hand or finger position data, as the participant must imagine movement trajectories while

following on-screen instructions (Fig 7a). During the task, multiunit threshold crossing data were recorded from the hand knob area. Remarkably, NMR successfully revealed single-trial latent dynamics without any overlap in trials that were 22.5 degrees apart (Fig 7b). The averaged 2D latent dynamics closely matched the imagined movement trajectories ($r^2 = 0.96$, based on hand positions). We optimized the hyperparameters of the three models before evaluating them across 20 runs (Fig 21). Consistent with the results obtained using actual hand positions, NMR also revealed aligned trajectories when trained on hand velocities (Fig 22a). While NMR outperformed both models, CEBRA showed better performance than pi-VAE but still lagged behind NMR (0.78, 0.59, and 0.23, Fig 7c). We observed similar results in the test trials and with the 3D versions of the CEBRA and pi-VAE models (Fig 22b). Consistent with earlier findings, NMR also had a shorter execution time compared to CEBRA (Fig 22c). Overall, NMR reveals the most aligned latent dynamics for attempted handwriting and shows strong potential for applications in brain-machine interfaces.

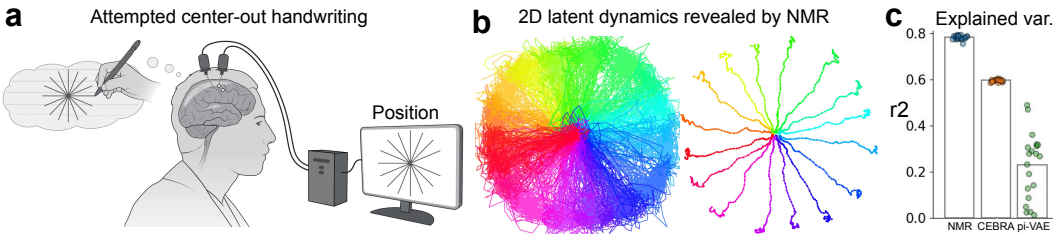

Figure 7: Dimensionality reduction on handwriting attempts in 16 directions. **a** A participant attempted to handwrite in 16 directions, following instructions displayed on a monitor. Neural recordings were made from two 96-channel Utah arrays implanted in the hand knob area of the precentral gyrus (modified from Willett et al. (2021)). **b** Single-trial and trial-averaged latent dynamics were revealed by NMR. **c** Explained variance of hand velocities across three models after 20 runs. Fig 21 shows hyperparameter tuning, and Fig 22 provides further comparison results.

5 Discussion

A benchmark of NMR against CEBRA and pi-VAE across multiple brain areas, four modalities of neural signals, and three movement tasks demonstrates NMR's superior performance in uncovering latent dynamics. One of the key strengths of NMR is its ability to extract nearly identical latent dynamics across different brain areas and over extended periods. This capability opens new avenues for both fundamental neuroscience research and brain-machine interface (BMI) applications. Previous studies by Gallego et al. (2020) and Safaie et al. (2023) revealed preserved latent dynamics across time and subjects performing similar behaviors using the PCA method. However, the latent dynamics revealed by NMR (as shown in Figs 1567) are significantly more informative than those uncovered by PCA. We believe NMR will help neuroscientists probe the stability of latent dynamics under various conditions. For BMI applications, we demonstrate that NMR, combined with a simple linear decoder, can predict hand movements across years, subjects, and hemispheres. This capability allows for training latent dynamics within and between subjects, enabling the prediction of movements in other subjects. The linear decoder's lack of hyperparameters is an additional advantage. Furthermore, NMR also revealed almost perfectly aligned 2D latent dynamics in a paralyzed human patient, further highlighting its potential for use in BMI applications for humans.

If the ultimate goal of a dimensionality reduction method is to align latent dynamics with any movements, then NMR is still far from achieving this. For the three movement tasks evaluated in this study, the movement trajectories are relatively simple. For complex movements like handwriting characters such as "m" or "k" (Willett et al., 2021), the latent dynamics will collapse. We believe this is due to the calculation of label distance; geodesic distance might be more suitable than Manhattan or Euclidean distance. Furthermore, we consider speech (Silva et al., 2024)—which involves coordinated movements of the jaw, tongue, lips, and larynx—to be one of the most challenging movement tasks. We believe it is still feasible to reveal the latent dynamics, though they are unlikely to be 2D, if the label distance of articulatory kinematic trajectories (AKTs) (Chartier et al., 2018) can be quantified. A model may need to reduce the dimensionality of both AKTs (coordinated movements in 13 dimensions) and neural dynamics.

REFERENCES

Antonis Antoniades, Yiyi Yu, Joseph Canzano, William Wang, and Spencer LaVere Smith. Neuroformer: Multimodal and multitask generative pretraining for brain data. *arXiv preprint arXiv:2311.00136*, 2023.

Mehdi Azabou, Mohammad Gheshlaghi Azar, Ran Liu, Chi-Heng Lin, Erik C Johnson, Kiran Bhaskaran-Nair, Max Dabagia, Bernardo Avila-Pires, Lindsey Kitchell, Keith B Hengen, et al. Mine your own view: Self-supervised learning through across-sample prediction. *arXiv preprint arXiv:2102.10106*, 2021.

Manuel Beiran, Nicolas Meirhaeghe, Hansem Sohn, Mehrdad Jazayeri, and Srdjan Ostojic. Parametric control of flexible timing through low-dimensional neural manifolds. *Neuron*, 111(5): 739–753, 2023.

Josh Chartier, Gopala K Anumanchipalli, Keith Johnson, and Edward F Chang. Encoding of articulatory kinematic trajectories in human speech sensorimotor cortex. *Neuron*, 98(5):1042–1054, 2018.

Hanbo Chen, Jiawei Yang, Daniel Iascone, Lijuan Liu, Lei He, Hanchuan Peng, and Jianhua Yao. Treemoco: contrastive neuron morphology representation learning. *Advances in Neural Information Processing Systems*, 35:25060–25073, 2022.

SueYeon Chung and Larry F Abbott. Neural population geometry: An approach for understanding biological and artificial neural networks. *Current opinion in neurobiology*, 70:137–144, 2021.

Mark M Churchland, John P Cunningham, Matthew T Kaufman, Justin D Foster, Paul Nuyujukian, Stephen I Ryu, and Krishna V Shenoy. Neural population dynamics during reaching. *Nature*, 487 (7405):51–56, 2012.

Uri Cohen, SueYeon Chung, Daniel D Lee, and Haim Sompolinsky. Separability and geometry of object manifolds in deep neural networks. *Nature communications*, 11(1):746, 2020.

John P Cunningham and Byron M Yu. Dimensionality reduction for large-scale neural recordings. *Nature neuroscience*, 17(11):1500–1509, 2014.

Jia Deng, Wei Dong, Richard Socher, Li-Jia Li, Kai Li, and Li Fei-Fei. Imagenet: A large-scale hierarchical image database. In *2009 IEEE conference on computer vision and pattern recognition*, pp. 248–255. Ieee, 2009.

Sven Dorkenwald, Peter H Li, Michał Januszewski, Daniel R Berger, Jeremy Maitin-Shepard, Agnes L Bodor, Forrest Collman, Casey M Schneider-Mizell, Nuno Maçarico da Costa, Jeff W Lichtman, et al. Multi-layered maps of neuropil with segmentation-guided contrastive learning. *Nature Methods*, 20(12):2011–2020, 2023.

Alexis Dubreuil, Adrian Valente, Manuel Beiran, Francesca Mastrogiuseppe, and Srdjan Ostojic. The role of population structure in computations through neural dynamics. *Nature neuroscience*, 25(6):783–794, 2022.

Juan A Gallego, Matthew G Perich, Raeed H Chowdhury, Sara A Solla, and Lee E Miller. Long-term stability of cortical population dynamics underlying consistent behavior. *Nature neuroscience*, 23 (2):260–270, 2020.

Cecilia Gallego-Carracedo, Matthew G Perich, Raeed H Chowdhury, Lee E Miller, and Juan Álvaro Gallego. Local field potentials reflect cortical population dynamics in a region-specific and frequency-dependent manner. *Elife*, 11:e73155, 2022.

Yuanjun Gao, Evan W Archer, Liam Paninski, and John P Cunningham. Linear dynamical neural population models through nonlinear embeddings. *Advances in neural information processing systems*, 29, 2016.

Richard J Gardner, Erik Hermansen, Marius Pachitariu, Yoram Burak, Nils A Baas, Benjamin A Dunn, May-Britt Moser, and Edvard I Moser. Toroidal topology of population activity in grid cells. *Nature*, 602(7895):123–128, 2022.

Erik Hermansen, David A Klindt, and Benjamin A Dunn. Uncovering 2-d toroidal representations in grid cell ensemble activity during 1-d behavior. *Nature Communications*, 15(1):5429, 2024.

Cole Hurwitz, Akash Srivastava, Kai Xu, Justin Jude, Matthew Perich, Lee Miller, and Matthias Hennig. Targeted neural dynamical modeling. *Advances in Neural Information Processing Systems*, 34:29379–29392, 2021.

Mehrdad Jazayeri and Srdjan Ostojic. Interpreting neural computations by examining intrinsic and embedding dimensionality of neural activity. *Current opinion in neurobiology*, 70:113–120, 2021.

Katarzyna Jurewicz, Brianna J Sleezer, Priyanka S Mehta, Benjamin Y Hayden, and R Becket Ebitz. Irrational choices via a curvilinear representational geometry for value. *Nature Communications*, 15(1):6424, 2024.

Mahsa Keramati, Lili Meng, and R David Evans. Conr: Contrastive regularizer for deep imbalanced regression. *arXiv preprint arXiv:2309.06651*, 2023.

Mohammad Reza Keshtkaran, Andrew R Sedler, Raeed H Chowdhury, Raghav Tandon, Diya Basrai, Sarah L Nguyen, Hansem Sohn, Mehrdad Jazayeri, Lee E Miller, and Chethan Pandarinath. A large-scale neural network training framework for generalized estimation of single-trial population dynamics. *Nature Methods*, 19(12):1572–1577, 2022.

Dmitry Kobak, Wieland Brendel, Christos Constantinidis, Claudia E Feierstein, Adam Kepecs, Zachary F Mainen, Xue-Lian Qi, Ranulfo Romo, Naoshige Uchida, and Christian K Machens. Demixed principal component analysis of neural population data. *elife*, 5:e10989, 2016.

Demetres Kostas and Frank Rudzicz. Thinker invariance: enabling deep neural networks for bci across more people. *Journal of Neural Engineering*, 17(5):056008, 2020.

Demetres Kostas, Stephane Aroca-Ouellette, and Frank Rudzicz. Bendr: Using transformers and a contrastive self-supervised learning task to learn from massive amounts of eeg data. *Frontiers in Human Neuroscience*, 15:653659, 2021.

Nina Kudryashova, Matthew G Perich, Lee E Miller, and Matthias H Hennig. Ctrl-tndm: Decoding feedback-driven movement corrections from motor cortex neurons. In *Computational and Systems Neuroscience (Cosyne) 2023*, 2023.

Patrick N Lawlor, Matthew G Perich, Lee E Miller, and Konrad P Kording. Linear-nonlinear-time-warp-poisson models of neural activity. *Journal of computational neuroscience*, 45:173–191, 2018.

Eric Kenji Lee, Hymavathy Balasubramanian, Alexandra Tsolias, Stephanie Udochukwu Anakwe, Maria Medalla, Krishna V Shenoy, and Chandramouli Chandrasekaran. Non-linear dimensionality reduction on extracellular waveforms reveals cell type diversity in premotor cortex. *Elife*, 10: e67490, 2021.

Ran Liu, Mehdi Azabou, Max Dabagia, Chi-Heng Lin, Mohammad Gheshlaghi Azar, Keith Hengen, Michal Valko, and Eva Dyer. Drop, swap, and generate: A self-supervised approach for generating neural activity. *Advances in neural information processing systems*, 34:10587–10599, 2021.

Leland McInnes, John Healy, and James Melville. Umap: Uniform manifold approximation and projection for dimension reduction. *arXiv preprint arXiv:1802.03426*, 2018.

Joseph E O'Doherty, Mariana MB Cardoso, Joseph G Makin, and Philip N Sabes. Nonhuman primate reaching with multichannel sensorimotor cortex electrophysiology. *Zenodo http://doi.org/10.5281/zenodo*, 583331, 2017.

Chethan Pandarinath, Daniel J O'Shea, Jasmine Collins, Rafal Jozefowicz, Sergey D Stavisky, Jonathan C Kao, Eric M Trautmann, Matthew T Kaufman, Stephen I Ryu, Leigh R Hochberg, et al. Inferring single-trial neural population dynamics using sequential auto-encoders. *Nature methods*, 15(10):805–815, 2018.

Felix Pei, Joel Ye, David Zoltowski, Anqi Wu, Raeed H Chowdhury, Hansem Sohn, Joseph E O'Doherty, Krishna V Shenoy, Matthew T Kaufman, Mark Churchland, et al. Neural latents benchmark'21: evaluating latent variable models of neural population activity. *arXiv preprint arXiv:2109.04463*, 2021.

Matthew G Perich, Juan A Gallego, and Lee E Miller. A neural population mechanism for rapid learning. *Neuron*, 100(4):964–976, 2018.

Lang Qian, Shengjie Zheng, Chunshan Deng, Cheng Yang, and Xiaojian Li. An adaptive contrastive learning model for spike sorting. *arXiv preprint arXiv:2205.11914*, 2022.

Mostafa Safaie, Joanna C Chang, Junchol Park, Lee E Miller, Joshua T Dudman, Matthew G Perich, and Juan A Gallego. Preserved neural dynamics across animals performing similar behaviour. *Nature*, 623(7988):765–771, 2023.

Omid G Sani, Hamidreza Abbaspourazad, Yan T Wong, Bijan Pesaran, and Maryam M Shanechi. Modeling behaviorally relevant neural dynamics enabled by preferential subspace identification. *Nature Neuroscience*, 24(1):140–149, 2021.

Steffen Schneider, Jin Hwa Lee, and Mackenzie Weygandt Mathis. Learnable latent embeddings for joint behavioural and neural analysis. *Nature*, 617(7960):360–368, 2023.

Xinke Shen, Xianggen Liu, Xin Hu, Dan Zhang, and Sen Song. Contrastive learning of subject-invariant eeg representations for cross-subject emotion recognition. *IEEE Transactions on Affective Computing*, 14(3):2496–2511, 2022.

Alexander B Silva, Kaylo T Littlejohn, Jessie R Liu, David A Moses, and Edward F Chang. The speech neuroprosthesis. *Nature Reviews Neuroscience*, pp. 1–20, 2024.

Wenbo Tang, Justin D Shin, and Shantanu P Jadhav. Geometric transformation of cognitive maps for generalization across hippocampal-prefrontal circuits. *Cell reports*, 42(3), 2023.

Carolina Urzay, Nauman Ahad, Mehdi Azabou, Aidan Schneider, Geethika Atamkuri, Keith B Hengen, and Eva L Dyer. Detecting change points in neural population activity with contrastive metric learning. In *2023 11th International IEEE/EMBS Conference on Neural Engineering (NER)*, pp. 1–4. IEEE, 2023.

Laurens Van der Maaten and Geoffrey Hinton. Visualizing data using t-sne. *Journal of machine learning research*, 9(11), 2008.

Ankit Vishnubhotla, Charlotte Loh, Akash Srivastava, Liam Paninski, and Cole Hurwitz. Towards robust and generalizable representations of extracellular data using contrastive learning. *Advances in Neural Information Processing Systems*, 36, 2023.

Binxu Wang and Carlos R Ponce. A geometric analysis of deep generative image models and its applications. In *International Conference on Learning Representations*, 2021. URL `https://openreview.net/forum?id=GH7QRzUDdXG`.

Francis R Willett, Donald T Avansino, Leigh R Hochberg, Jaimie M Henderson, and Krishna V Shenoy. High-performance brain-to-text communication via handwriting. *Nature*, 593(7858): 249–254, 2021.

Wannan Yang, Chen Sun, Roman Huszár, Thomas Hainmueller, Kirill Kiselev, and György Buzsáki. Selection of experience for memory by hippocampal sharp wave ripples. *Science*, 383(6690): 1478–1483, 2024.

Yuzhe Yang, Kaiwen Zha, Yingcong Chen, Hao Wang, and Dina Katabi. Delving into deep imbalanced regression. In *International conference on machine learning*, pp. 11842–11851. PMLR, 2021.

Han Yu, Hanrui Lyu, Ethan YiXun Xu, Charlie Windolf, Eric Kenji Lee, Fan Yang, Andrew M Shelton, Shawn Olsen, Sahar Minavi, Olivier Winter, et al. In vivo cell-type and brain region classification via multimodal contrastive learning. *bioRxiv*, pp. 2024–11, 2024.

Ding Zhou and Xue-Xin Wei. Learning identifiable and interpretable latent models of high-dimensional neural activity using pi-vae. *Advances in Neural Information Processing Systems*, 33:7234–7247, 2020.

Feng Zhu, Harrison A Grier, Raghav Tandon, Changjia Cai, Anjali Agarwal, Andrea Giovannucci, Matthew T Kaufman, and Chethan Pandarinath. A deep learning framework for inference of single-trial neural population dynamics from calcium imaging with subframe temporal resolution. *Nature neuroscience*, 25(12):1724–1734, 2022.

A Appendix

A.1 Contrastive learning in neuroscience

A.1.1 Studies that neglect imbalanced labels

There has been a surge in the development of contrastive learning methods for neural data. Some of these methods do not face class imbalance issues because they address tasks where imbalance is not a concern, such as change point detection (Urzay et al., 2023), generating neural activity to predict behavior (Antoniades et al., 2023), and behavior decoding (Azabou et al., 2021). For cell-type classification, which inherently involves imbalanced classes, previous studies have not explicitly addressed the class imbalance problem. For instance, (Yu et al., 2024) proposed the multimodal NEMO model for cell-type and brain region classification. While they acknowledged the imbalance by reporting macro-averaged F1 scores and balanced accuracy, they did not provide solutions to mitigate the issue. Similarly, (Vishnubhotla et al., 2023) introduced CEED for spike sorting and cell-type classification without mentioning the class imbalance, despite its prevalence in neural cell types. Moreover, other studies have applied contrastive learning to neurophysiological data such as spike sorting without considering class imbalance. (Vishnubhotla et al., 2023) also used CEED for spike sorting without mentioning the class imbalance issue. (Qian et al., 2022) applied contrastive learning for spike sorting but did not consider class imbalance. (Chen et al., 2022) proposed TreeMoCo for neural morphology representation learning but did not consider the inherent imbalance of neural types in the brain.

In summary, most previous studies applying contrastive learning to neuroscience—whether on time-series data or images—do not consider or attempt to address imbalanced labels.

A.1.2 Studies that address imbalanced labels

Among the contrastive learning studies in neuroscience that address imbalanced labels, we found all rely on traditional sampling techniques focused on discrete classes. For example: (Dorkenwald et al., 2023) proposed SegCLR for connectomics data. They mentioned: "Examples were rebalanced class-wise by upsampling all classes to match the most numerous classes. During testing, imbalances between classes were balanced by repeating examples from minority classes." (Kostas & Rudzicz, 2020) mentioned: "Wherever there was an imbalance in examples between classes, we under-sampled the majority class(es)..." (Kostas et al., 2021) mentioned: "The P300, ERN, and SSC datasets all had imbalanced class distributions; during training, we adjusted for these imbalances by undersampling points uniformly of the more frequent classes..." (Shen et al., 2022) mentioned: "The neutral emotion category was not included in the basic version due to an unbalanced number of trials (only four trials for eliciting neutral emotion)."

We are the first to address imbalanced labels for time-series neural data, and also the first to do so without adding or removing any data samples, achieving an 80-100% performance gain over previous SOTA methods.

A.2 Code

Operating system: Ubuntu 22.04.3 LTS, GPU: NVIDIA RTX A5000, CPU: Intel Xeon W-2225.

We have uploaded all of our code, including the modified loss function, preprocessing scripts, and figure generation code. We modified only four files in the "cebra" code folder. The latest CEBRA version that we used was released on January 10, so all files except these four have a modified date

of January 10. The modified files include two in the data folder (single_session.py and datatypes.py) and two in the solver folder (single_session.py and base.py). We revised three of four files for data sampling (retain continuous labels) as follows:

In single_session.py (Lines 69-71, 76-79), we retained continuous labels for computing the ConR loss later on. Notably, NMR and CEBRA both utilize continuous labels in continuous.py within the "distribution" folder, which we did not modify.

Lines 69-71 for extracting continuous labels and ConR parameters from inputs

```
XY_position = self.continuous_index[:, 0:2]
Z_target = self.continuous_index[:, 2][index.reference]
para = self.continuous_index[0:4, 3]
```

Lines 76-79 for retaining continuous labels

```
index_ref = XY_position[index.reference, 0],
index_pos = XY_position[index.reference, 1],
Z_target = Z_target,
para = para
```

We commented out two lines (Line 75 and 260) because the computation of the ConR loss does not require the embeddings or indices of negative samples extracted by CEBRA.

```
negative=self[index.negative],
negative_idx = reference_idx[num_samples:]
```

Original file for reference:

https://github.com/AdaptiveMotorControlLab/CEBRA/blob/main/cebra/data/single_session.py#

In datatypes.py (Lines 55-58 and 64-67 to add labels, and Lines 54 and 63 to comment out negative samples), we used this file to retain the continuous labels, serving a similar purpose as single_session.py. Original file for reference:

https://github.com/AdaptiveMotorControlLab/CEBRA/blob/main/cebra/data/datatypes.py#L46

In the solver folder, single_session.py (Lines 72-76 for adding labels and Line 71 for commenting out negative samples) also retains the continuous labels but on the GPU, fulfilling the same function as the files above. Original file for reference:

https://github.com/AdaptiveMotorControlLab/CEBRA/blob/main/cebra/solver/single_session.py#L59

The computation of ConR loss is implemented in base.py in the solver folder. This file contains two key parts: Target label prediction (Lines 346-356), where we use linear regression on the CPU with scikit-learn. ConR loss calculation (Lines 61-163), where we use two embeddings, real and predicted labels, and two parameters. Original file for reference:

https://github.com/AdaptiveMotorControlLab/CEBRA/blob/main/cebra/solver/base.py#L225

A.3 InfoNCE vs ConR loss

The computation of InfoNCE loss contains these key five lines of code:

```
# feature similarity of all positive and negative samples
1. pos_dist = einsum("nd,nd->n", ref, pos)/tau
2. neg_dist = einsum("nd,md->nm", ref, neg)/tau
# attract similar samples
3. pos_loss = -pos_dist.mean()
# repel dissimilar samples
```

```
4. neg_loss = logsumexp(neg_dist, dim = 1).mean()
# minimize this loss during in each epoch
5. loss = pos_loss + neg_loss
```

The computation of ConR loss contains these key ten lines of code:

```
# feature similarity of all samples
1. logits = - (features[:, None, :] - features[None, :, :])
        .norm(2, dim=-1).div(t)
# find positive pairs, I_dist is the true pairwise distance,
# w is distance threshold
2. pos_i = l_dist.le(w)
# find negative pairs, p_dist is the the predicted distance
3. neg_i = ((~(l_dist.le(w))) * (p_dist.le(w)))
# feature similarity of positive samples
4. pos = torch.exp(logits * pos_i)
# feature similarity of negative samples
5. neg = torch.exp(logits * neg_i)
# pushing weight
6. pushing_w = inverse_freq * torch.exp(l_dist_XY * e) * neg_i
# denominator (equation on the right)
7. neg_exp_dot = (pushing_w * neg).sum(1)
# denominator
8. loss_single_denom = (pos.sum(1) + neg_exp_dot).unsqueeze(-1)
# single sample ConR loss (numerator/denominator)
9. loss_single = torch.div(pos, loss_single_denom)
# sum and averaged over all samples in the batch
10. loss = (-torch.log(loss_single) * pos_i).sum(1)
        / (pos_i.sum(1)).mean()
```

A.4 SAMPLING

A.4.1 NEGATIVE SAMPLING

The key difference between two losses is the selection of negative samples, which are dependent and independent of behavioral labels in NMR and CEBRA, respectively (Fig 8a). Here, we put the codes and their links of negative sampling in CEBRA when supervised with continuous labels.

```
https://github.com/AdaptiveMotorControlLab/CEBRA/blob/main/cebra/
data/single_session.py#L162
```

L162 class ContinuousDataLoader(cebra_data.Loader): "Contrastive learning conditioned on a continuous behavior variable."

```
https://github.com/AdaptiveMotorControlLab/CEBRA/blob/main/cebra/
data/single_session.py#L249
```

```
# call \sample_prior" function in continuous.py file
    in the \distributions" folder
L249 reference_idx = self.distribution.sample_prior(num_samples*2)
L250 negative_idx = reference_idx[num_samples:]
L251 reference_idx = reference_idx[:num_samples]
```

```
https://github.com/AdaptiveMotorControlLab/CEBRA/blob/main/cebra/
distributions/continuous.py#L34
```

class Prior(abc_.PriorDistribution, abc_.HasGenerator):"An empirical prior distribution for continuous datasets."

```
https://github.com/AdaptiveMotorControlLab/CEBRA/blob/main/cebra/
distributions/continuous.py#L52
```

```
def sample_prior(self, num_samples: int, offset:
```

```
Optional[Offset] = None) -> torch.Tensor:
"Return uniformly sampled indices."
# random integers from low to high
return self.randint(self.offset.left, self.num_samples -
        self.offset.right, (num_samples,))
```

The CEBRA paper (5th paragraph of Methods/Sampling) also stated that "In the simplest case, negative sampling returns a random sample from the empirical distribution by returning a randomly chosen index from the dataset."

It's important to note that most supervised contrastive learning methods guide negative sampling based on labels, but CEBRA does not employ this approach—it uses unsupervised negative sampling. Similarly, NMR does not use labels to guide sampling; instead, it utilizes labels later in computing the ConR loss.

A.4.2 POSITIVE SAMPLING

NMR used the same positive samples extracted by CEBRA.

```
https://github.com/AdaptiveMotorControlLab/CEBRA/blob/main/cebra/
data/single_session.py#L252
```

This indices of positive samples are assigned in this line:

```
positive_idx = self.distribution.sample_conditional(reference_idx)
```

This function will call "sample_conditional" from "TimedeltaDistribution" class in continuous.py file in the "distributions" folder:

```
https://github.com/AdaptiveMotorControlLab/CEBRA/blob/main/cebra/
distributions/continuous.py#L200
```

This is where "TimedeltaDistribution" is defined which will define a conditional distribution based on continous behavioral changes over time:

```
class TimedeltaDistribution():
self.data = continuous # continuous movements labels
self.time_difference[time_delta:] = (self.data[time_delta:]
    - self.data[:-time_delta])
self.index = cebra.distributions.ContinuousIndex(self.data)
```

It will call the ContinuousIndex function in the index.py file of the same folder

```
https://github.com/AdaptiveMotorControlLab/CEBRA/blob/main/cebra/
distributions/index.py#L131
```

This is where "ContinuousIndex" is defined:

```
class ContinuousIndex(distributions.Index):
def search(self, query):
distance = self.dist_matrix(query),
return torch.argmin(distance, dim=0)
```

It will call "DistanceMatrix" that is defined in:

```
https://github.com/AdaptiveMotorControlLab/CEBRA/blob/main/cebra/
distributions/index.py#L55
```

It will use most naive neighbor search implementation that involves the brute-force computation of distances between all pairs of points in the dataset.

```
class DistanceMatrix(cebra.io.HasDevice):
```

This is where "sample_conditional" is defined:

```
https://github.com/AdaptiveMotorControlLab/CEBRA/blob/main/cebra/
distributions/continuous.py#L240


def sample_conditional(self, reference_idx)-> torch.Tensor:
    num_samples = reference_idx.size(0)
# return random integers
diff_idx = self.randint(len(self.time_difference), (num_samples,))
# time-offset to reference as positive samples
query = self.data[reference_idx] + self.time_difference[diff_idx]
# call the search function mentioned earlier
return self.index.search(query)
```

A.4.3 IMPROVEMENTS ON SAMPLING BY CONR LOSS

Strictly speaking, our sampling approach is similar to that of CEBRA. We agree with the reviewer that "removing the negative sample batch and replacing it with movement labels does not appear novel." However, our key improvement lies in how we compute the ConR loss, where we determine negative samples supervised by labels. Broadly speaking, we enhance the sampling process by effectively filtering out unintended negative samples from the original set of positive samples extracted by CEBRA. Here's a detailed explanation:

In the CEBRA paper, the authors state: For a continuous context variable c_t, we can use a set of time offsets Δ to specify the distribution. Given the time offsets, the empirical distribution $P(c_{t+\tau} \mid c_t)$ for a particular choice of $\tau \in \Delta$ can be computed from the dataset: we build up a set $D = \{t \in [T], \tau \in \Delta : c_{t+\tau} - c_t\}$, sample a d uniformly from D, and obtain the sample that is closest to the reference sample's context variable modified by this distance $(c + d)$ from the dataset.

In practice, this involves the following key code snippets from CEBRA's implementation:

```
https://github.com/AdaptiveMotorControlLab/CEBRA/blob/main/cebra/
distributions/continuous.py#L228


self.data = continuous # continuous movement labels
self.time_delta = time_delta # time offsets
self.time_difference = torch.zeros_like(self.data,
    device=self.device)
# computing label difference d
self.time_difference[time_delta:] = (self.data[time_delta:]
    - self.data[:-time_delta])
# add the d back to c get query (c + d)
query = self.data[reference_idx]
    + self.time_difference[diff_idx]
```

The problem arises when the continuous labels are imbalanced, as is often the case with movement labels. In such scenarios, labels can quickly transition to infrequent values and then revert back to more frequent ones. When this happens, the computed $(c + d)$, which is intended to index positive (or augmented) samples relative to the anchor after a time offset, may inadvertently point to negative samples. This occurs because the nearest neighbor search retrieves a sample whose label is closest to $(c + d)$, but due to label imbalance, this sample might actually belong to a different class (i.e., a negative sample) (Fig 8a).

As a result, some negative samples are inadvertently mixed into the set of positive samples extracted by CEBRA. Our method addresses this issue by filtering out these unintended negative samples through supervised labels during the computation of the ConR loss (Fig 8b).

In summary, although our initial sampling approach mirrors that of CEBRA, during the computation of the ConR loss we improve negative sampling by selecting samples supervised by labels, and we improve positive sampling by filtering out unintended negative samples.

A.5 PARAMETERS AND HYPERPARAMETERS

All parameters and hyperparameters for our models are presented in the seven main figures, the thirteen supplementary figures, and summarized Table 1. Additionally, since all training was done in Jupyter Notebook, the hyperparameters are also saved there. Please note that the input data for both NMR and CEBRA are identical. For NMR and CEBRA, no validation data is used; instead, an 80/20 split is applied for training and testing. In contrast, the pi-VAE model uses a 60/20/20 split for training, validation, and testing. pi-VAE was executed on a CPU due to issues with an older version of TensorFlow, which is why we did not compare its execution time with that of NMR and CEBRA. The execution time refers to the training or model fitting time and is associated with the following line of code for both CEBRA and NMR:

```
model.fit(neural, continuous_index)
```

The inference time corresponds to the line of code:

```
model.transform(neural)
```

It converts raw neural dynamics into latent dynamics. This operation is performed on a CPU and takes approximately 0.1 seconds, being similar for both models.

Table 1: Parameters and hyperparameter for NMR and CEBRA models. The XY coordinates represent either hand positions (Figures 1 and 7) or velocities (Figures 2–6). Note that hand reaching angles range from 0 to 360 degrees, but the XY coordinates (maxXY) have different units—such as cm/s or m/s—and may represent different metrics like position or velocity. Since we need to sum the absolute distances of the X-coordinate, Y-coordinate, and angle, we multiply the XY coordinates by a scale factor (XY2Z). This means smaller XY coordinates will have a larger magnification, and vice versa. ITR: iterations, BS: batch size, LR: learning rate, TEMP: temperature τ, maxXY: maximum values of X and Y coordinates, XY2Z: magnification ratio of XY coordinates, PCG: precentral gyrus.

Figure	**ITR (1K)**	**BS**	**LR**	**TEMP**	**maxXY**	**XY2Z**
1_S1 positions_NMR	20	512	0.001	0.045	13	50
2_M1_NMR	10	512	0.001	0.07	33	10
2_M1_CEBRA	5	512	0.001	0.08	33	10
2_PMd_NMR	5	512	0.001	0.08	33	10
2_PMd_CEBRA	10	512	0.001	0.08	33	10
4_M1_NMR	5	512	0.001	0.065	33	10
4_M1_CEBRA	5	512	0.001	0.1	33	10
4_PMd_NMR	5	512	0.001	0.065	33	10
4_PMd_CEBRA	5	512	0.001	0.1	33	10
5_M1 sort_NMR	10	512	0.001	0.06	0.2	2000
5_M1 sort_CEBRA	10	512	0.005	0.1	0.2	2000
5_M1 unsort_NMR	10	512	0.0005	0.06	0.2	2000
5_M1 unsort_CEBRA	10	512	0.0005	0.1	0.2	2000
6_M1+PMd_NMR	10	512	0.0001	0.08	31	10
6_M1+PMd_CEBRA	10	512	0.0001	1	31	10
7_PCG positions_NMR	10	512	0.0001	0.06	4	100
7_PCG positions_CEBRA	10	512	0.0001	0.1	4	100

A.6 DATASETS

We have evaluated in a total of 1+28+37+1+1+=68 sessions in the main results.

To test the generalizability of our model, we first evaluated it on neural recordings from the rat hippocampus (Fig. 9). We used data from Rat Cicero because it is highly imbalanced, with minutes of pausing at the ends of the track. The data will be automatically downloaded in the CEBRA software package.

Eight direction center-out reaching (Fig 1): 1 monkey, 1 session

The neural data was recorded from Somatosensory cortex. The data will be downloaded in the CEBRA software package automatically.

Eight direction center-out reaching (Fig 234): 2 monkeys, 28 sessions

`https://datadryad.org/stash/dataset/doi:10.5061/dryad.xd2547dkt`

This data is released accompanying this paper Gallego-Carracedo et al. (2022):

`https://elifesciences.org/articles/73155#data`

The data is Matlab format and we extract following information: tgtDir (Target direction, radians for Monkey Chewie and Mihali), idx-goCueTime (The time go Cue is one), vel(XY velocities), M1-spikes for both Chewie 2015 and Chewie 2016, and PMd-spikes only for Chewie 2016. The time bin is 30ms and we extract all the spikes after each go Cue. We extracted 40 bins for both monkeys. We smoothed the discrete spike count in the Matlab using a Gaussian kernel. The standard deviation is 1.5 and kernel size is six standard deviations. We keep all the trials and neurons.

Natural movements in 9 x 9 Grid (Fig 5) (O'Doherty et al., 2017):1 monkey, 37 sessions

`https://zenodo.org/records/583331`

Natural movements with random targets (Fig 6) (Lawlor et al., 2018): 1 monkey, 1 session

`https://crcns.org/data-sets/motor-cortex/pmd-1/about-pmd-1`

We used the first session of Monkey MM that performed 496 trials of reaching tasks. There are 67 neurons in M1 and 94 neurons in PMd.

Human Handwriting (Fig 7) (Willett et al., 2021): 1 patient, 1 session

`https://datadryad.org/stash/dataset/doi:10.5061/dryad.wh70rxwmv`

A.7 Mathematical details

Consider a training dataset consisting of N examples, which we denote as $\{(x_i, y_i)\}_{i=0}^{N}$, where $x_i \in \mathbb{R}^d$ is a neural data input, and $y_i \in \mathbb{R}^{d'}$ is its corresponding label. Here, d is the dimension of the input—that is, the raw dimensionality of neural signals or dynamics—which could be the number of simultaneously recorded single units, multi-units, or electrode channels. The value of d' is the dimension of the supervised continuous movement labels. In this study, $d' = 3$, comprising either velocity or position along the X-coordinate, velocity or position along the Y-coordinate, and angle. For the hippocampus dataset, the labels include the animal's location and two values indicating left and right direction. For the movement labels, their distribution $\mathcal{D}_y$ deviates significantly from a uniform distribution (highly imbalanced).

Each neural data sample x_i is passed through the feature encoder $\mathcal{E}(\cdot)$ to obtain the neural embedding $v_i \in \mathbb{R}^{d''}$, where the dimensionality of the latent dynamics d'' is predetermined. The objective is to train a feature encoder $\mathcal{E}(\cdot)$ such that the embeddings v_i are organized both spatially and temporally to correspond to their labels y_i.

Let $d(\cdot, \cdot)$ represent the distance measure between two labels. The ground truth sample label is y and predicted sample label is $\hat{y}$. For each anchor sample i, the positive samples are those that satisfy $d(y_i, y_p) < \hat{d}$, the negative samples are those that satisfy $d(y_i, y_n) > \hat{d}$ and $d(\hat{y_i}, \hat{y_n}) < \hat{d}$, where $\hat{d}$ is the median of all pairwise distance shown in Fig 1e.

Let's denote v_i, v_p, and v_n as the neural embeddings of corresponding true labels of y_i, y_p, and y_n. N_i^+ is the number of positive samples, N_i^- is the number of negative samples. $K_i^+ = \{v_p\}_p^{N_i^+}$ is the set of embeddings from positive samples, $K_i^- = \{v_n\}_n^{N_i^-}$ is the set of embeddings from negative samples. $sim(\cdot, \cdot)$ is the similarity measure between two feature embeddings (e.g. negative L_2 norm). For each anchor i whose neural embedding is v_i, true label is y_i, and loss is:

$$\mathcal{L}_{\text{ConR}_j} = \frac{1}{N_i^+} \sum_{v_j \in K_i^+} -\log \frac{\exp(sim(v_i, v_j)/\tau)}{\sum_{v_p \in K_i^+} \exp(sim(v_i, v_p)/\tau) + \sum_{v_n \in K_i^-} S_{i,n} \exp(sim(v_i, v_n)/\tau)} \tag{1}$$

where τ is a temperature hyperparameter and $S_{i,n}$ is a pushing weight for each negative pair shown in Fig 1f:

$$S_{i,n} = \frac{1}{p_{d(y_i, y_n)}} exp(d(y_i, y_n)\tau) \tag{2}$$

where $\frac{1}{p_{d(y_i, y_n)}}$ is the inverse frequency of labels distances distribution shown in Fig 1c. The final loss is the summed and averaged loss $\mathcal{L}_{\text{ConR}_j}$ over all anchors i in a batch:

$$\mathcal{L}_{\text{ConR}} = \frac{1}{2N} \sum_{j=0}^{2N} \mathcal{L}_{\text{ConR}_j} \tag{3}$$

For each anchor i whose neural embedding is v_i, the InfoNCE loss used by CEBRA is:

$$\mathcal{L}_{\text{InfoNCE}_j} = -\log \frac{\exp(sim(v_i, v_j)/\tau)}{\sum_{n=1}^{N} \exp(sim(v_i, v_n)/\tau)} \tag{4}$$

where v_i, v_j, and v_n are the anchor, positive, and negative samples, respectively. There are four major differences between the InfoNCE loss in CEBRA and the ConR loss in NMR:

First, only one positive sample v_j is used in ConR loss, instead of multiple v_j that belong to K_i^+.

Second, in InfoNCE loss, negative samples are drawn from the entire batch of samples, whereas in ConR loss, only negative samples from K_i^- are selected.

Third, InfoNCE loss does not include a regularizer for negative samples, while ConR loss uses $S_{i,n}$ as a regularizer (to apply pushing weights).

Fourth, InfoNCE loss does not require labels, whereas ConR loss requires labels y_i and y_n for both the anchor and negative samples.

Together, our simplified loss function does not introduce any additional hyperparameters.

A.8 Decoding cross multi-sessions

For training model cross multiple sessions, the model needs to be trained separately for each session or animal. We achieved this by iterating through all datasets in the designated folder. In the uploaded Jupyter Notebooks, all .ipynb files that have "batch" in their name indicate they are designed for multi-session training. For example, the file "Fig2_NMR_SU_Batch_PMd.ipynb" trains the NMR model on all neural data from PMd.

In the Fig 3, which presents the cross-session decoding experiment. In this experiment, the only fine-tuning performed was rotating the angles of the latent dynamics. This was necessary because, in some sessions, the angles of the extracted latent dynamics were rotated by 45 degrees or flipped relative to the ground truth movement trajectories. To address this, we used the orthogonal Procrustes method from SciPy:

`https://docs.scipy.org/doc/scipy/reference/generated/scipy.linalg.orthogonal_procrustes.html`

Using this method, we selected a target angle and rotated the entire 3D latent dynamics with the computed orthogonal matrix. This alignment preserves local details and the relative positions of each reaching direction. Once all latent dynamics were aligned with their corresponding movements, we trained a linear regression decoder on 80% of the training data from one session and used it to decode movements in other sessions with the 20% held-out test data. This information has been added to the revised manuscript.

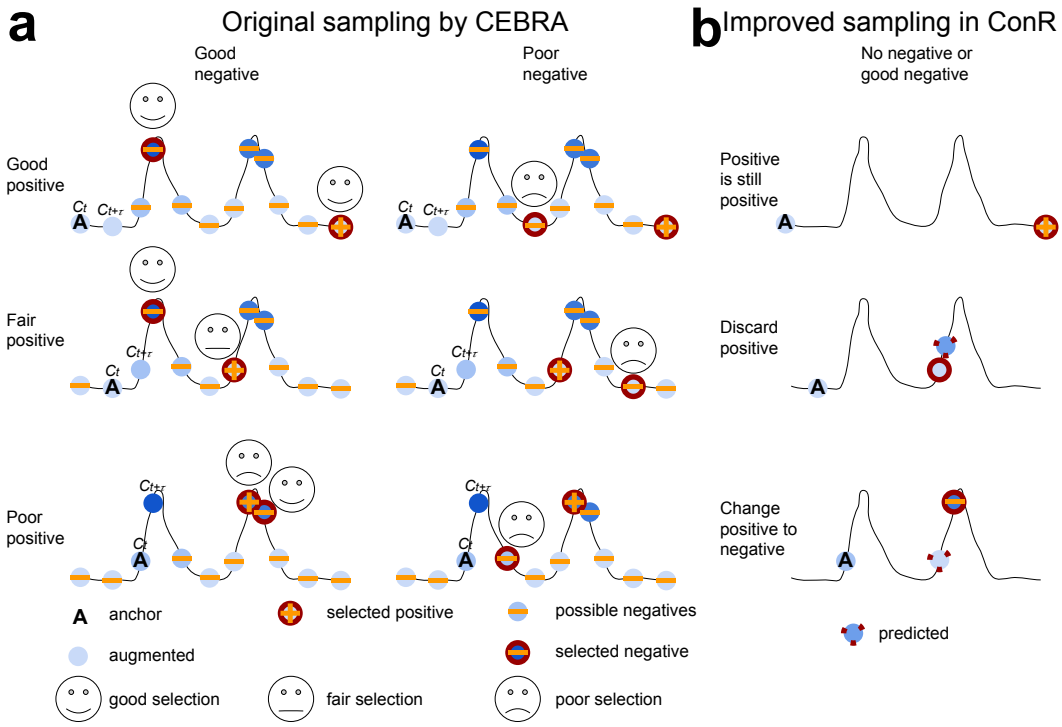

Figure 8: Original and Improved Sampling Strategies. **a** Depending on the position where the anchor ("A") sample falls on the continuous label C_t, the label of the augmented sample $C_{t+\tau}$ could be similar (first row), slightly different (second row), or very different (third row). The positive sample ("+") will have a label that is closest to the augmented sample. Therefore, if the augmented sample changes rapidly relative to the anchor sample, the selection of positive samples may be fair or poor. Since negative sampling is uniform and unsupervised, negative samples (denoted by "-") could appear in many positions. They might fall into a continuous label that is supposed to be very different from the anchor (first column) or, incorrectly, into a position similar to the anchor (second column). **b** NMR does not require negative samples for computing the ConR loss. Instead, it refines the original positive samples extracted by CEBRA. There are three situations: 1) No change needed: If the originally selected positive sample is close to the anchor within a distance threshold (first row). 2) Discarded: If it is far away from the anchor and the predicted label is also far away. 3) Changed to negative sample: If the true label is far from the anchor but predicted to be close. For simplicity in visualization, we show only one anchor, one negative, and one positive sample. In the actual experiment, there are 512 samples for each type. In the computation of the ConR loss, each anchor sample is compared with 512 positive samples to classify those samples into positive, negative, or discarded.

Table 2: Datasets information for decoding across sessions, hemispheres, animals, and years related to Fig 3. n/a: no recordings in the PMd of right hemisphere.

Date	Monkey	Hemisphere	Trial	M1	PMd
140217	Mihili	Right	208	44	104
140218	Mihili	Right	225	38	121
140303	Mihili	Right	208	52	66
140304	Mihili	Right	203	39	76
140306	Mihili	Right	217	43	86
140307	Mihili	Right	216	26	66
150313	Chewie	Right	1038	86	n/a
150309	Chewie	Right	1026	72	n/a
150629	Chewie	Right	179	49	n/a
150630	Chewie	Right	178	44	n/a
160929	Chewie	Left	208	74	114
161005	Chewie	Left	202	82	167
161006	Chewie	Left	209	63	192
161007	Chewie	Left	168	70	137
161014	Chewie	Left	740	88	190
161021	Chewie	Left	286	84	211

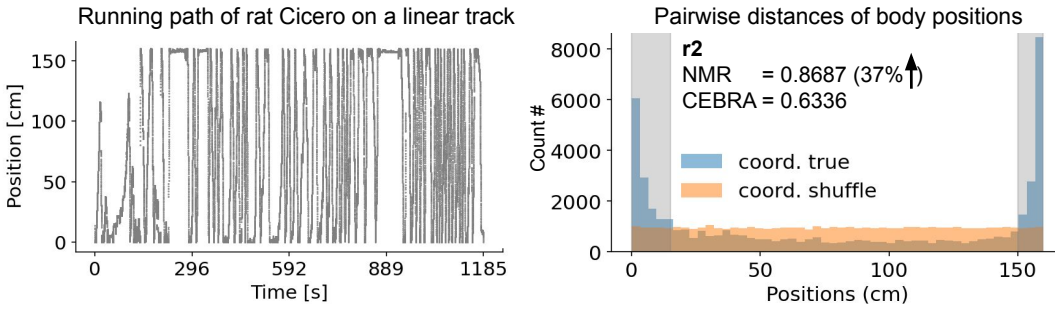

Figure 9: Model evaluation was conducted on body movement tasks using neural data from free-moving rats. Left: Multi-channel electrophysiological recordings were collected while a rat traversed a 1.6 m linear track either "leftward" or "rightward." It is worth noting that the rat occasionally paused at the ends of the track, resulting in data imbalance. Right: Pairwise distances between samples from the entire body movement trajectories reveal a highly imbalanced distribution. At both the beginning (0–15 cm) and the end (150–160 cm) of the track, significantly more data were collected compared to the shuffled condition (beginning: 27% vs. 9%; end: 27% vs. 6%). Two-dimensional latent dynamics were extracted using NMR and CEBRA and employed to predict movements through linear regression. The explained variance (r^2) of body movements was 37% higher with NMR compared to CEBRA. Both models were optimized via hyperparameter searches for learning rate and temperature.

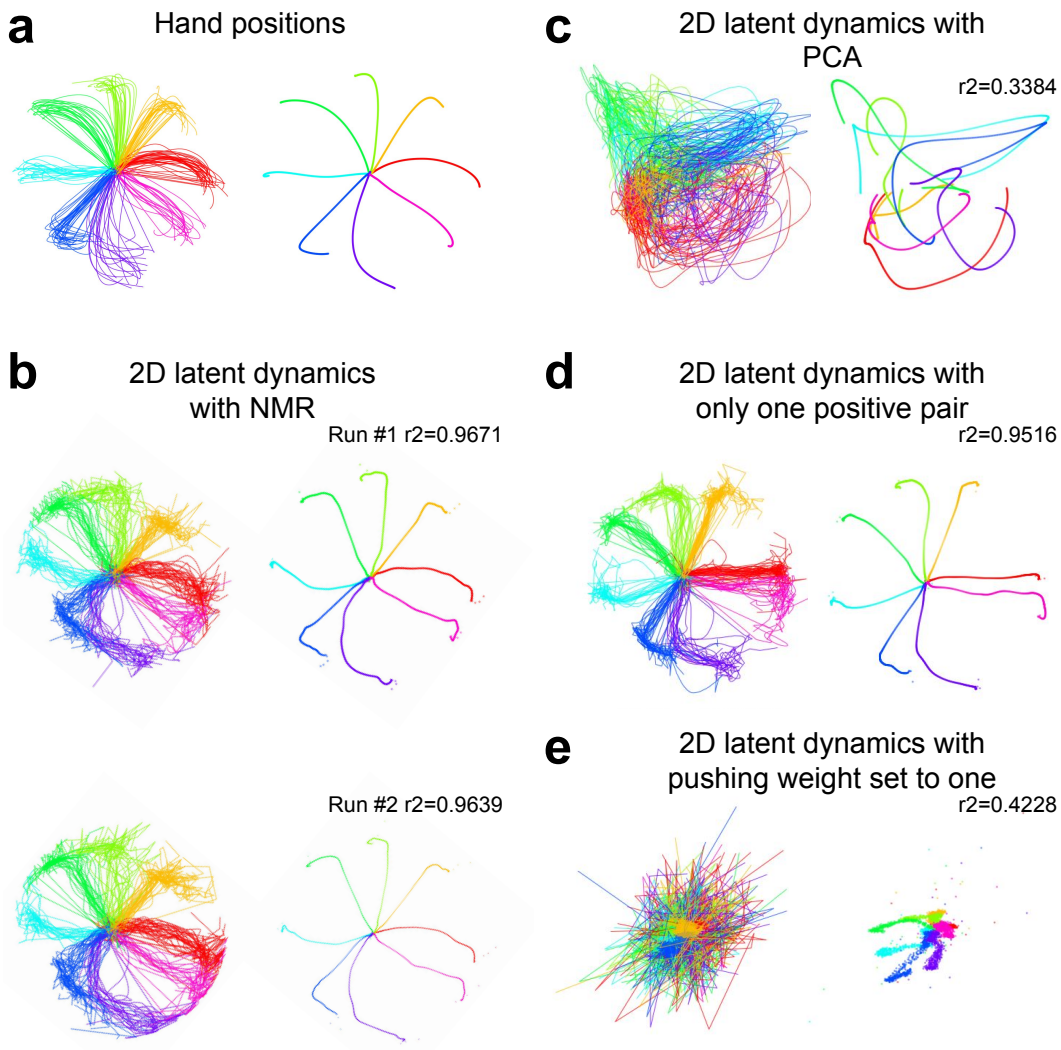

Figure 10: Single-trial and trial-averaged hand positions and latent dynamics. **a** Ground truth movement trajectories. **b** Two additional examples of Fig 1b (right panel). **c** 2D latent dynamics extracted using PCA applied to raw 65D neural signals. **d** 2D latent dynamics extracted with NMR, containing only one positive pair (i.e., its own augmented sample with the same label and zero distance to the anchor sample). **e** 2D latent dynamics extracted with NMR, with the pushing weight $S_{i,n}$ set to one.

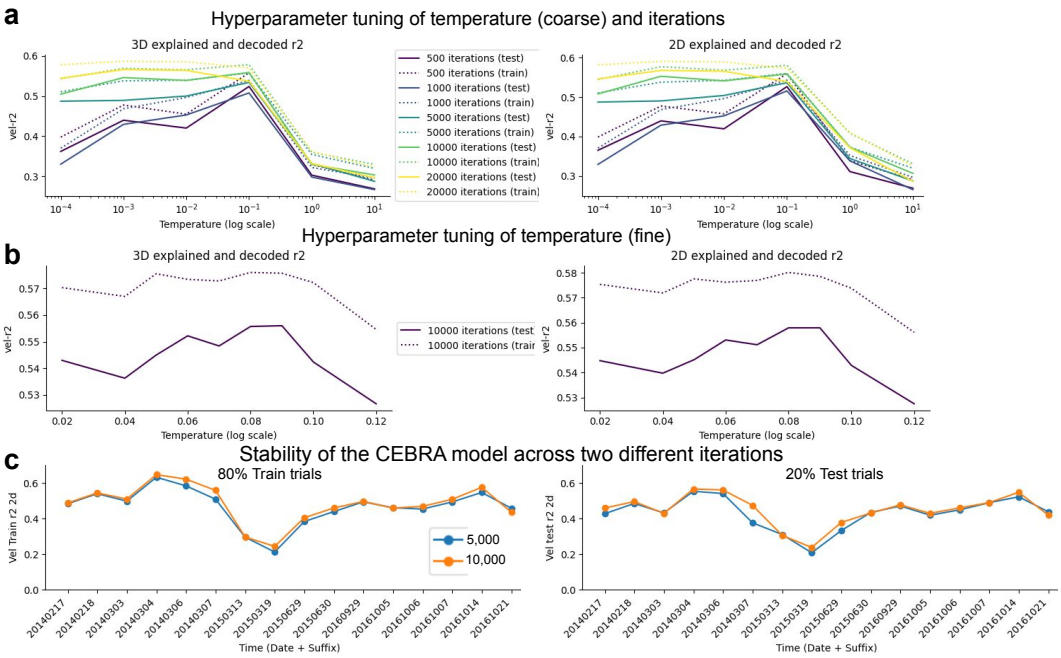

Figure 11: Hyperparameter tuning and stability of CEBRA. **a**. Hyperparameter search across five different iterations and six different temperatures. The evaluated session is from Monkey C (20161014, M1). **b**. A finer hyperparameter search at 10,000 iterations. **c**. Explained variance (left) and decoded variance (right) at two different iteration numbers across 14 sessions in M1.

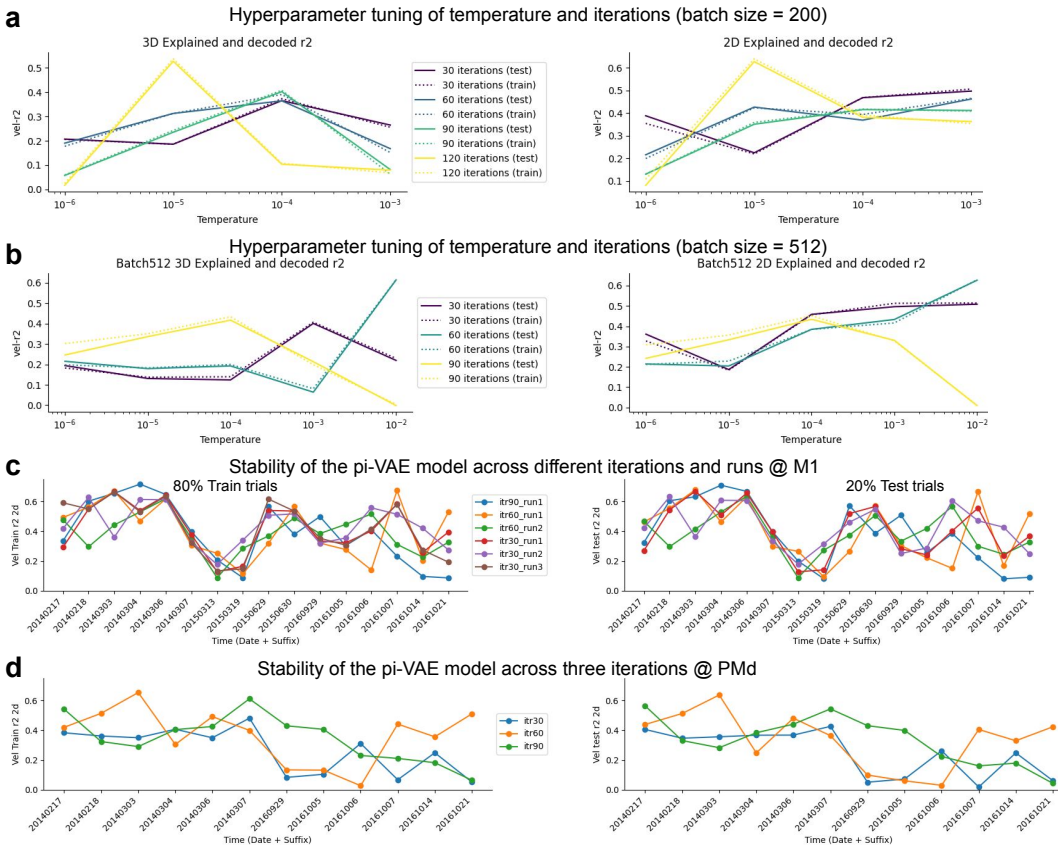

Figure 12: Hyperparameter tuning and stability of pi-VAE. **a**. Hyperparameter search across four different iterations and four different learning rates. The evaluated session is from Monkey C (20161014, M1). **b**. Similar search, but using a larger batch size. **c**. Explained and decoded variance under different iteration numbers and across multiple runs. Note that the performance shows a similar trend across sessions but has larger variability within each session. **d**. Similar to panel c, but models are evaluated in PMd.

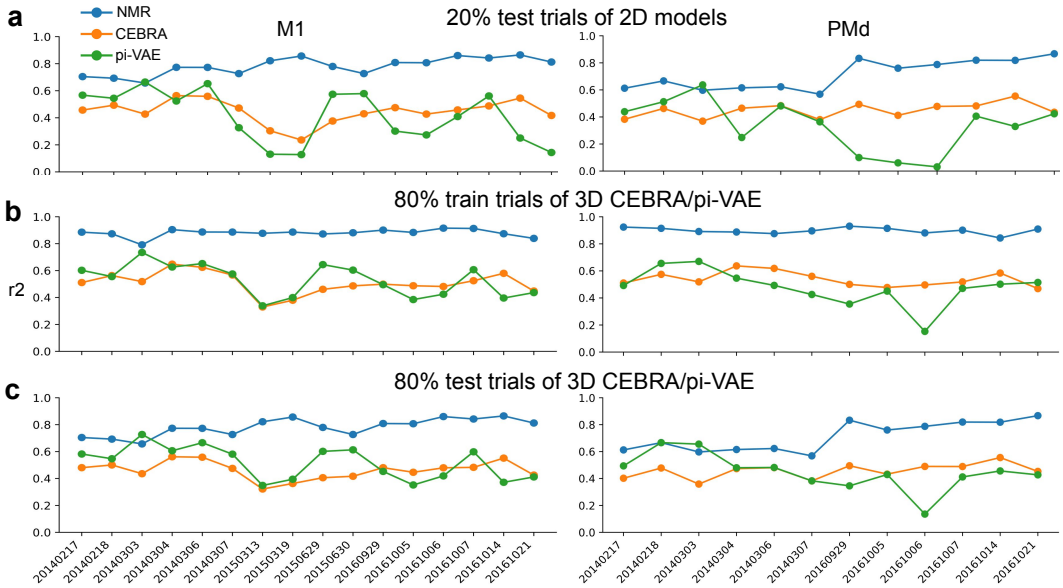

Figure 13: Test trial performance and 3D model comparison. Same format as Figure 2, but for held-out 20% test trials using 3D CEBRA and pi-VAE models. **a**. Decoded r² across sessions in M1 and PMd using 2D models. **b**. Explained r² and **c**. Decoded r² for 2D NMR compared to 3D CEBRA and 3D pi-VAE models.

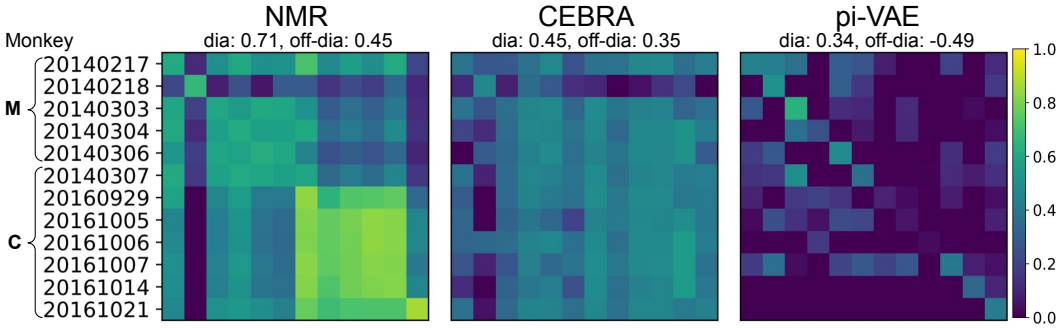

Figure 14: Decoding results in PMd, following the same format as Fig 3. The t-statistics and p-values for the diagonal values are 10.1821 and 1.9e-06 (NMR vs CEBRA), 5.0372 and 1.1e-03 (NMR vs pi-VAE), 1.8407 and 0.2783 (CEBRA vs pi-VAE). The t-statistics and p-values for the off-diagonal values are 6.5845 and 3.0e-09 (NMR vs CEBRA), 6.2945 and 1.3e-08 (NMR vs pi-VAE), 5.7219 and 2.0e-07 (CEBRA vs pi-VAE).

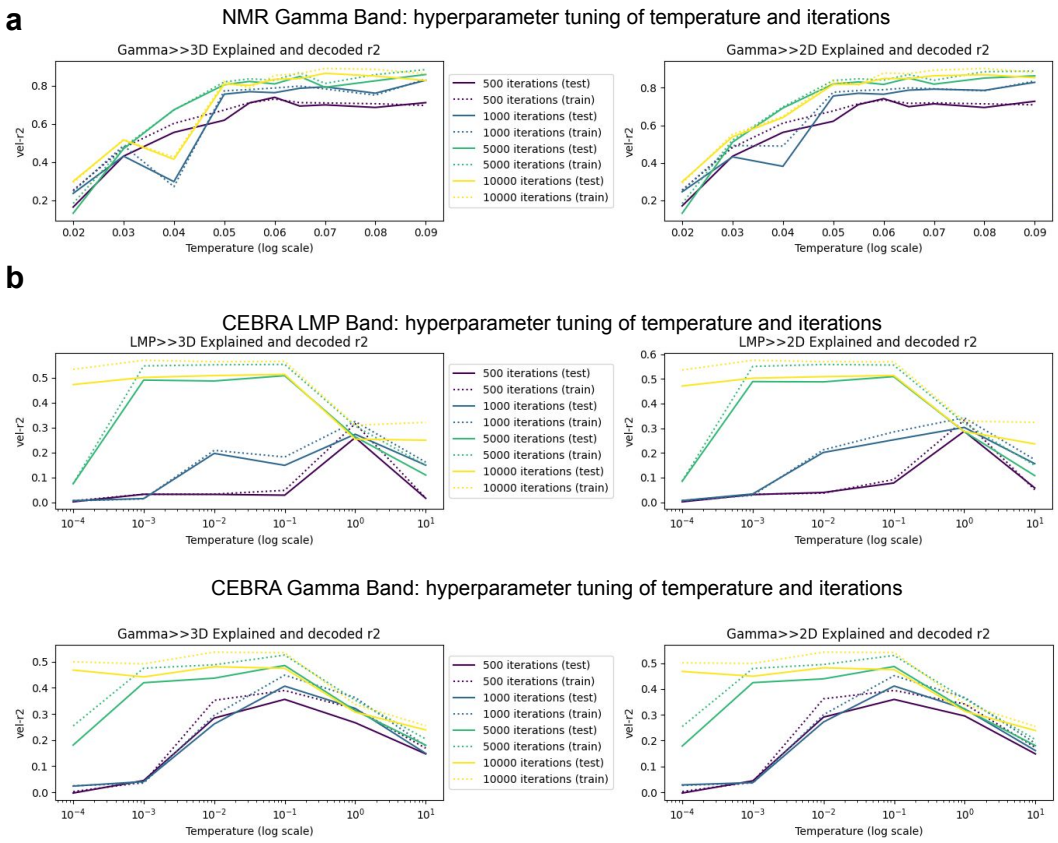

Figure 15: Hyperparameter tuning for two models. **a**. Explained variance across four iterations and eight temperatures in the high Gamma band (200-400 Hz) for NMR. **b**. Similar tuning results for CEBRA in the LMP (smoothed LFP signals) and Gamma bands.

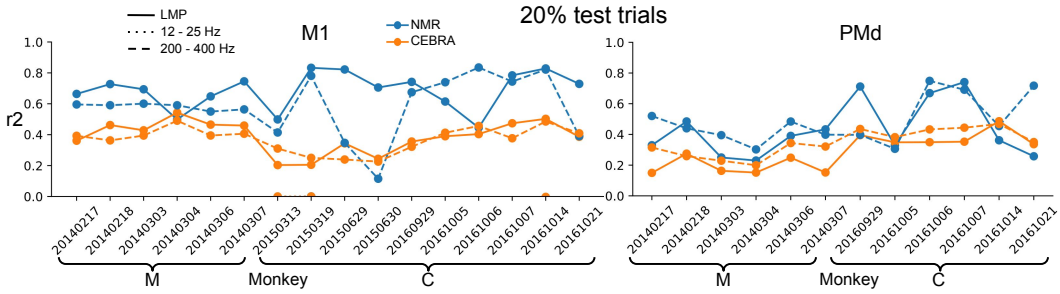

Figure 16: Decoding performance on held-out test trials, following the same format as Fig 4.

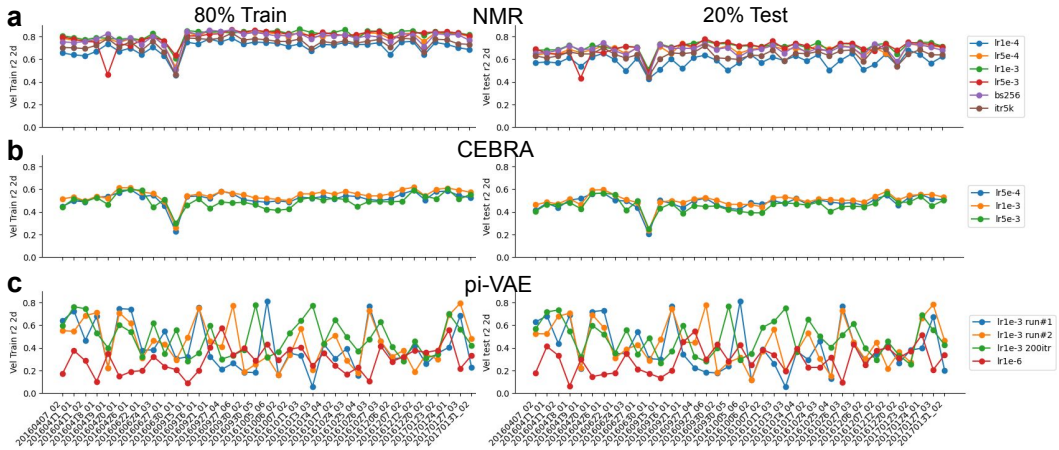

Figure 17: Explained variance under different hyperparameters. **a**. Variance results for four different learning rates, smaller batch sizes (256 vs. 512), and fewer iterations (5,000 vs. 10,000). **b**. Results for three different learning rates. **c**. Comparison between two runs using the same learning rate but higher iterations (200 vs. 100) and a much lower learning rate.

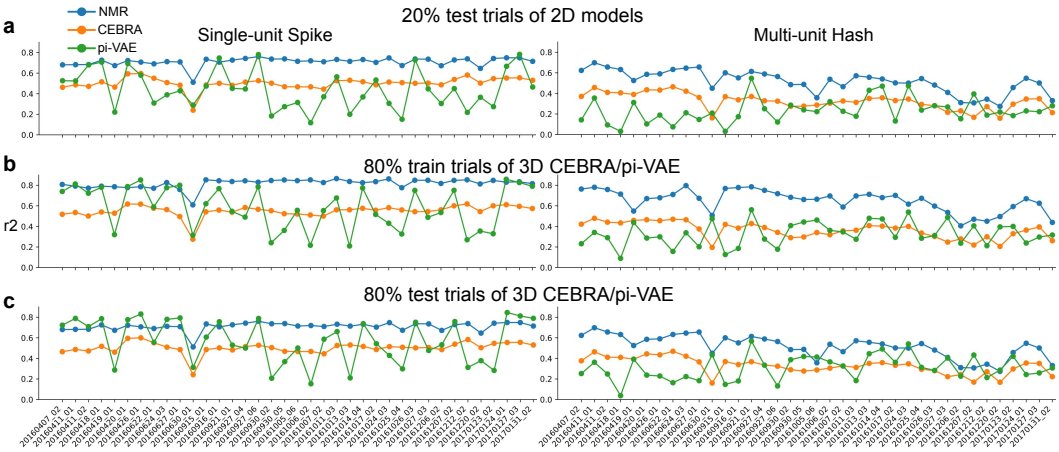

Figure 18: Decoding performance for test trials (**a**) and 3D CEBRA/pi-VAE models (**b**, **c**).

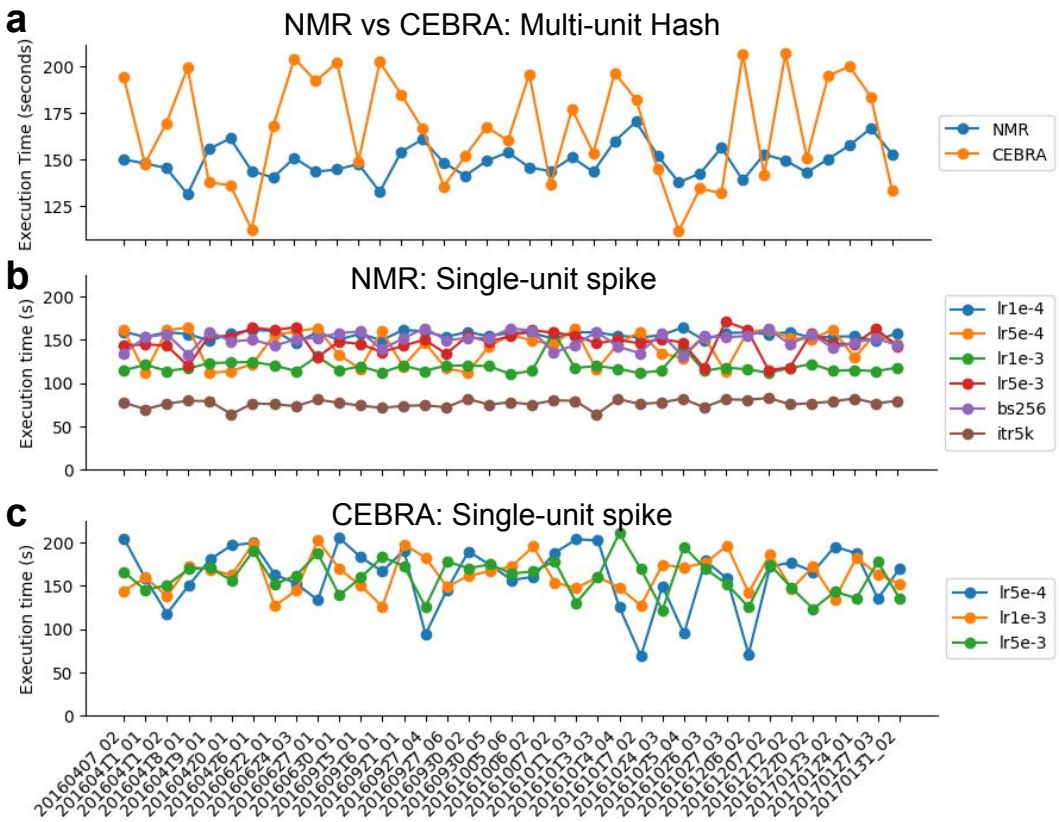

Figure 19: Execution time for NMR and CEBRA models. **a**. Same format as Figure 5f, but for unsorted events. **b**. Comparison of execution times for four different learning rates, smaller batch sizes, and fewer iterations. **c**. Execution time results for three different learning rates.

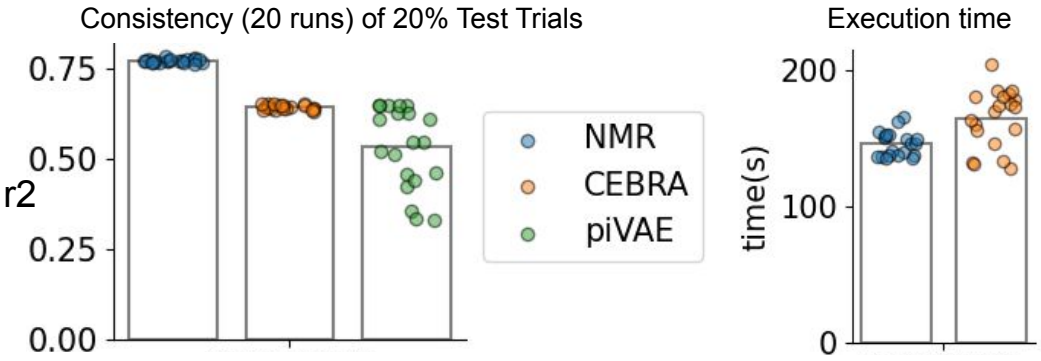

Figure 20: Model decoding performance in the testing trials and execution times.

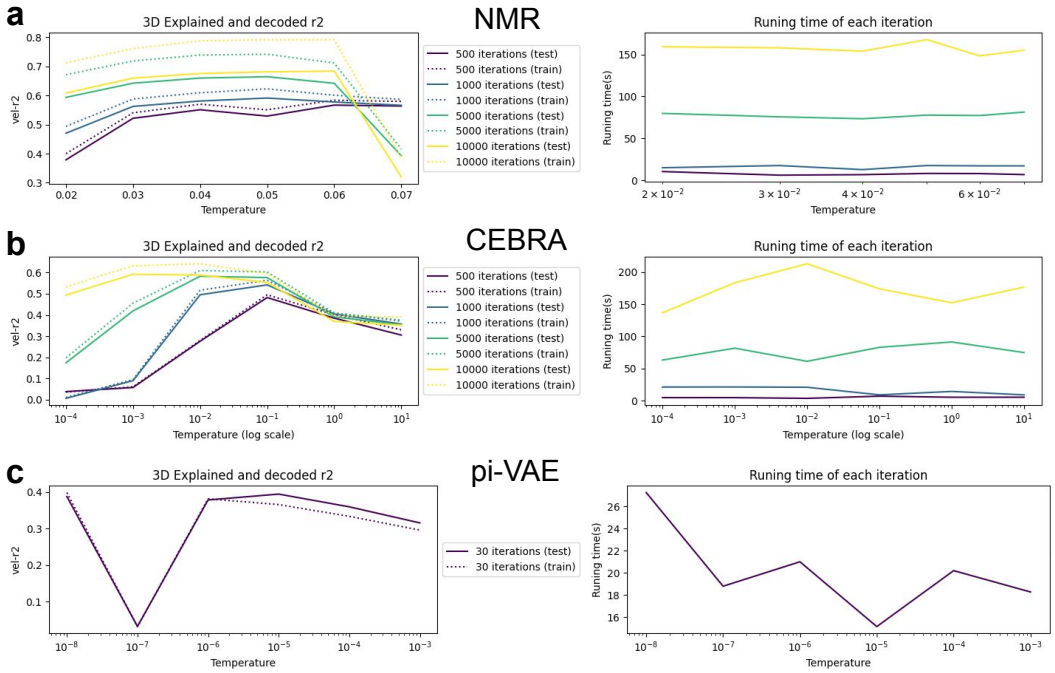

Figure 21: Hyperparameter search and runtime of NMR (**a**), CEBRA (**b**), and pi-VAE (**c**) models

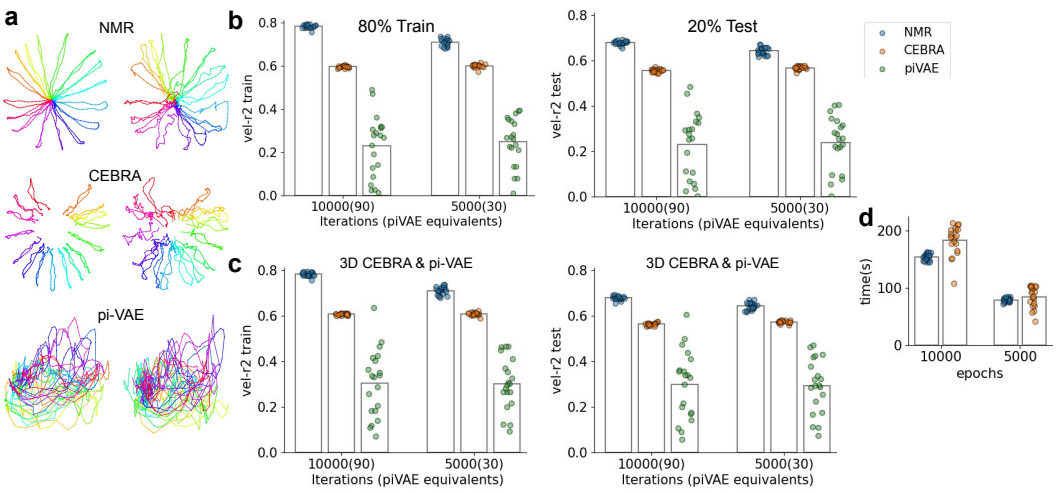

Figure 22: 2D latent dynamics of the three models and performance across different conditions. **a**. 2D latent dynamics in training trials (left) and held-out test trials (right). **b**. Explained variance of hand velocities in training and test trials at two sets of iterations. **c**. Similar analysis for 3D CEBRA and pi-VAE models. **d**. Execution time comparison between NMR and CEBRA at two different iteration levels.